Natural Resources Research, Vol. 31, No. 1, February 2022 (© 2022)
https://doi.org/10.1007/s11053-021-09986-3

Original Paper

Comparison of Pore Size Distribution, Heterogeneity and Occurrence Characteristics of Movable Fluids of Tight Oil Reservoirs Formed in Different Sedimentary Environments: A Case Study of the Chang 7 Member of Ordos Basin, China

Qibiao Zang,[1,2] Chenglin Liu,[1,2,3] Rizwan Sarwar Awan,[1,2] Xiya Yang,[1,2] Zhendong Lu,[1,2] Guoxiong Li,[1,2] Yuping Wu,[1,2] Dehao Feng,[1,2] and Yu Ran[1,2]

Received 30 June 2021; accepted 14 November 2021
Published online: 12 January 2022

The complexity and diversity of reservoir characteristics, including strong heterogeneity, complex pore structures, distinct pore size distributions, and various fluid occurrences, in different environments lead to differential oil recovery from the Chang 7 reservoir. In this research, several experiments such as nuclear magnetic resonance, high-pressure mercury intrusion, scanning electron microscopy, thin section, and X-ray diffraction were utilized to analyze PSD, heterogeneity, and movable fluid occurrence in the Chang 7 sandstone samples from the Ansai and Heshui Blocks. A 3-stage construction method is proposed to transform the T_2 spectrum to pore-throat radius distribution to realize large-scale and continuous PSD characterization. The results indicate that the sandstone in the Heshui Block is mainly feldspar lithic fragment sandstone, while the sandstone in the Ansai Block is mainly lithic fragment feldspar sandstone and feldspar sandstone. The storage spaces in the Chang 7 reservoirs were comprised primarily of nanoscale pores, followed by submicron pores. The Chang 7 reservoirs in different environments differed greatly in PSD, fractal feature, and movable fluid occurrence. Sandstone in the Heshui Block, compared to that in the Ansai Block, had better physical properties generally characterized by more submicron pores, weak heterogeneity, and more movable fluid in submicron pores. The movable fluid occurrence could be affected by various factors such as physical properties, mineral composition, pore size and distribution, and heterogeneity. The influence of these factors on movable fluid distribution varied in reservoirs of different areas. Generally, reservoirs with good physical properties and higher availability of submicron pores are often associated with high movable fluid content. The influence of carbonatite on the movable fluid content in the two areas was opposite. The relationship between the movable fluid content in different pores and pore size parameters varied in different sedimentary environments. The influence of heterogeneity on the movable fluid occurrence in submicron pores was stronger than nanoscale pores in the Heshui Block, while it was the opposite in the Ansai Block.

[1]State Key Laboratory of Petroleum Resource and Prospecting, China University of Petroleum, Beijing 102249, China.
[2]College of Geosciences, China University of Petroleum, Beijing 102249, China.
[3]To whom correspondence should be addressed; e-mail: lclzgx@126.com

KEY WORDS: Tight reservoirs, Pore size distribution, Movable fluid, Fractal dimension, Nuclear magnetic resonance.

INTRODUCTION

Global energy demand is increasing rapidly with the depletion of conventional petroleum reservoirs (Law & Curtis, 2002; Jia et al., 2012). Scholars pay more and more attention to unconventional petroleum resources in energy structure to fulfill the energy demand (Law & Curtis, 2002; Shanley et al., 2004; Tahir et al., 2020; Awan et al., 2021). Globally, the massive occurrence of oil reserves in tight sandstone reservoirs has attracted many scholars and experts' attention in their exploration (Taylor et al., 2010; Worden et al., 2018; Dai et al., 2019; Loucks & Dutton, 2019; Zhang et al., 2020a). The horizontal well multistage fracturing technology is useful in evaluating the commercial development of tight sandstone oil (Li et al., 2018b; Tian et al., 2018). In China, tight oil reservoirs are defined as reservoirs with an in situ permeability of less than 0.1×10^{-3} μm^2 and porosity of less than 10% (Jia et al., 2012; Zou et al., 2012). Tight oil reservoirs are featured by the complex micro/-nanoscale pore structure, weak permeation and storage capacity, low petroleum recovery, and strong heterogeneity. These characteristics are significantly different from conventional sandstone reservoirs (Clarkson et al., 2012a, 2012b; Lai et al., 2018a; Oluwadebi et al., 2019; Qiao et al., 2020a; Nie et al., 2021).

Ordos Basin is China's largest production base of low permeability and tight sandstone oil and gas (Liu & Yang, 2000; Yang et al., 2005; Hou et al., 2021). During the depositional period of the Chang 7 Member, a set of thick oil source rocks were deposited in the Ordos Basin, which laid the foundation for oil generation in Mesozoic continental basins (Yuan et al., 2015; Fu et al., 2018). The sedimentary environment during the deposition of the Chang 7 Member in the Heshui Block was quite different from that in the Ansai Block. In the Heshui Block, the Chang 7 Member comprises semi-deep lacustrine gravity flow deposits, mainly in the forms of sandy and muddy debris gravity flow channels (Yuan et al., 2015; Fu et al., 2018). However, in the Ansai Block, the Chang 7 Member is a typical delta front deposit, and the sand bodies are mainly in the forms of subaqueous distributary channels (Yuan et al., 2015). The pore size distribution (PSD) and pore structure heterogeneity (PSH) affect the storage and permeation capacity of a tight oil reservoir. The reservoirs formed in different sedimentary settings could have diverse PSD and PSH. In addition, various types and degrees of diagenesis would further increase the differences in PSD and pore structure of tight oil reservoirs (Lai et al., 2016; Qiao et al., 2020b; Zou et al., 2020). Therefore, tight oil reservoirs formed in different environments have various storage and permeation capacities, resulting in great differences in development measures.

Fluids in pores of tight oil reservoirs include movable fluids and bound fluids (Timur, 1969; Al-Mahrooqi et al., 2003; Li et al., 2019b; Wang & Zeng, 2020). The free state fluids in the interconnected pores are movable fluids, which is the only valuable resource in a tight oil reservoir. However, due to the fluid and the capillary interaction, the fluid in tiny pores is in the bound state, and these fluids are called bound fluids. The pore-throat size, heterogeneity, and PSD are important factors that affect the flow capacity of movable fluids. Movable fluids in large pores and throats usually have strong fluidity. Movable fluid porosity and saturation are important parameters for evaluating movable fluid content, reflecting movable fluid distribution characteristics in pores (Gao & Li, 2015; Tian et al., 2019). The occurrence characteristics of the movable fluid in tight oil reservoirs vary significantly under different sedimentary environments, resulting in great differences in oil recovery. Therefore, it is essential to pay special attention to PSD, heterogeneity, and movable fluid occurrence in tight oil reservoirs formed in different sedimentary environments.

Several techniques can be used to analyze the PSD and pore structure of sandstone; for example, high-pressure mercury intrusion (HPMI), X-ray computed tomography (CT), constant pressure mercury intrusion (CPMI), scanning electron microscopy (SEM), and thin section (Al-Mahrooqi et al., 2006; Desbois et al., 2011; Schmitt Rahner et al., 2018; Shabaninejad et al., 2018; Loucks & Dutton, 2019; Wu et al., 2019, 2021; Thomson et al.,

2020; Zhao et al., 2021). SEM can be used to analyze qualitatively pore-throat radius distribution, pore-throat morphology, and the occurrence patterns of clay minerals. The information of surface porosity, pore-throat coordination number, debris composition, and the pore combination form can be obtained from thin sections (Desbois et al., 2011; Wu et al., 2019). Mercury injection technology can be used characterize quantitatively the PSD by capillary curve and related pore structure parameters, such as pore-throat size, sorting, connectivity, and permeability (Eslami et al., 2013; Loucks & Dutton, 2019; Rezaee et al., 2012). CPMI is an effective technique for identifying pores and throats of different sizes (Yao & Liu, 2012). CT can be used to reconstruct the three-dimensional spatial distribution of PSD (Shabaninejad et al., 2018). Scholars have praised nuclear magnetic resonance (NMR) technology in reservoir evaluation because of its rapid and non-destructive advantages (Carr et al., 1996; Al-Mahrooqi et al., 2003, 2006; Yao et al., 2010; Wu et al., 2019; Zhang et al., 2019b, 2020). Previous studies have proved that NMR can be used to analyze effectively tight oil reservoirs' fluid occurrence and pore structure (Al-Mahrooqi et al., 2003; Eslami et al., 2013; Zhou et al., 2016a; Lyu et al., 2018; Sun et al., 2019; Wang et al., 2021). Many studies have transformed the T_2 spectrum into pore-throat radius distribution based on the high-pressure mercury intrusion (HPMI) test. It makes continuous and multiscale testing possible in reservoir microscopic characteristics evaluation (Al-Mahrooqi et al., 2006; Dai et al., 2019; Huang et al., 2020). The continuous improvements in NMR technology gradually achieve high-precision characterization of PSD and fluid occurrence characteristics. Additionally, fractal analysis is a crucial method for understanding the heterogeneity of rock (Mandelbrot et al., 1984; Katz & Thompson, 1985; Zhang & Andreas, 2014; Lai et al., 2018a; Wu et al., 2021). Fractal dimension is an important parameter for analyzing rock features. The fractal dimension of sandstone is distributed between 2 and 3, reflecting overall heterogeneity of pore structure. The closer the fractal dimension is to 3, the stronger the heterogeneity of sandstone.

Great progress has been made in the classification of micro-pore structure of tight sandstone, and in fluid mobility evaluation (Taylor et al., 2010; Deveugle et al., 2014; Hingerl et al., 2016; Schmitt et al., 2016; Mozley et al., 2016; Li et al., 2018a; Loucks & Dutton, 2019; Zha et al., 2019; Li et al., 2020; Liu et al., 2020a). However, most previous studies failed to consider the influence of the sedimentary environment on PSD and PSH in a tight oil reservoir. In addition, research on differences in PSD and movable fluid occurrence in reservoirs formed in different sedimentary environments has not attracted enough attention. Therefore, taking the Chang 7 Member as an example, this paper compared quantitatively the differences in PSD, heterogeneity, movable fluid occurrence, and influential factors of tight oil reservoir formed in different sedimentary environments using NMR, HPMI, SEM, thin section, and X-ray diffraction (XRD). This study provides a scientific basis for improving oil recovery.

GEOLOGICAL BANKGROUND AND SAMPLES

The Ordos Basin is a superimposed craton depression basin, which is considered to be an essential petroliferous basin in China (Liu & Yang, 2000). It can be divided into six first-order tectonic units, namely Yimeng uplift, Weibei uplift, Jinxi flexure belt, Yishan slope, Tianhuan depression, and West Rim thrust belt. The Heshui and Ansai Blocks are located in the tectonic unit of the Yishan Slope (Fig. 1) (Liu & Yang, 2000; Yang et al., 2005). The Chang 7 Member of the Upper Triassic Yanchang Formation is rich in tight oil and gas resources and is considered a target layer. The structure of the target layer in the Heshui and Ansai Blocks is gentle. In the Heshui Block, the Chang 7 Member is in the form of a typical semi-deep lacustrine sedimentary system (Zhou et al., 2016b; Cui et al., 2019b). Its provenance comes from the southwest and south, and the sand bodies of gravity flow origin are interbedded with adjacent source rock. In the Ansai Block, the Chang 7 Member is in the form of a typical delta front sedimentary system (Fu et al., 2018; Cui et al., 2019b). Its provenance comes from the north and northeast. The rocks of the Chang 7 Member in the study area are composed mainly of sandstone, argillaceous sandstone, sandy mudstone, grey mudstone, and black shale (Lai et al., 2016; Cui et al., 2019a). The characteristics of the Chang 7 sandstone are: (1) fine grain size; (2) complex mineral composition; (3) strong heterogeneity; and (4) poor petrophysical properties.

There are differences in rock types in the Heshui and Ansai Blocks. The former comprises mainly feldspathic lithic fragment sandstone, while the lat-

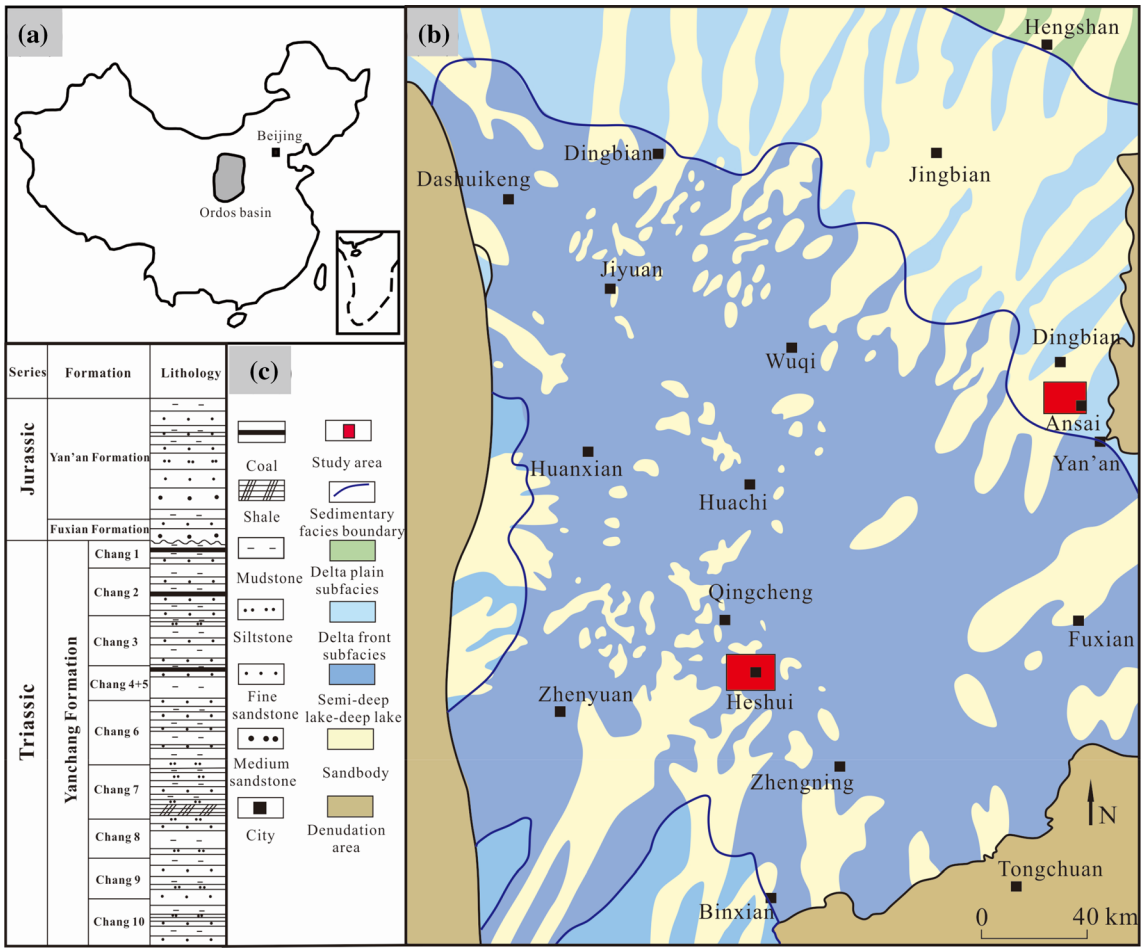

Figure 1. (**a**) Geographic location of the Ordos Basin in China. (**b**) Locations of the Ansai Block and Heshui Block in the Ordos Basin. (**c**) Lithologic column of the Yanchang Formation.

ter comprises primarily lithic fragment feldspar sandstone and feldspar sandstone. Inter-granular and intra-granular dissolution pores, residual inter-granular pores, and inter-crystalline pores are the main pore types of the Chang 7 sandstone. A few micro-fractures are found in some sandstone samples, and most of them are related to diagenesis and sedimentation.

For this study, 16 sandstone samples were drilled for NMR test as well as other supporting tests including physical properties, casting thin sections, SEM, HPMI, and XRD, to analyze the PSD and movable fluid occurrence. The parameters of NMR samples are shown in Table 1. In addition, other data were collected and used to support this study, including physical property data of 2049 samples, thin sections of 475 samples, SEM of 86 samples, and XRD of 86 samples.

The mineral composition of the Chang 7 sandstone samples was analyzed quantitatively by XRD. The mineral compositions mainly include quartz, feldspar, and clay (Table 2). The mineral composition in the Heshui Block was significantly different from that in the Ansai Block. In the Heshui Block, quartz content was distributed between 45.4 and 58.9%, with average of 53.6%. The feldspar content ranged mainly from 16.9 to 27.0% (average 21.5%). Clay content was low, ranging from 10.7 to 20.7%

Table 1. Parameters of NMR samples from the Chang 7 sandstone reservoir

Block	No	Well	Depth (m)	$T_{2cutoff}$ (ms)	Porosity (%)	Permeability ($\times 10^{-3}$ μm^2)	Movable fluid saturation (%)	Movable fluid porosity (%)	Bound water saturation (%)
Heshui	#1	L23	1645.40	10.015	11.82	0.1500	47.38	5.60	52.62
	#2	L23	1672.03	12.028	7.87	0.0240	39.25	3.36	60.75
	#3	L205	1636.90	6.255	10.04	0.0500	44.16	4.70	55.84
	#4	L205	1645.20	12.898	13.67	0.0400	49.03	6.20	50.97
	#5	L181	1613.60	1.746	4.87	0.0880	42.51	2.34	57.49
	#6	Z143	1842.67	20.371	7.87	0.0240	40.66	2.99	59.34
	#7	Z225	1772.90	19.957	12.44	0.0230	47.73	5.67	52.27
	#8	Z225	1775.04	4.069	1.81	0.0020	17.03	0.53	82.97
Ansai	#9	Q71	1434.54	2.797	5.97	0.0026	18.21	1.51	81.79
	#10	Q168	1664.00	4.338	9.22	0.0200	51.68	5.80	48.32
	#11	G62	1603.15	3.724	7.23	0.0199	52.44	2.57	47.56
	#12	G62	1606.28	39.101	9.75	0.1148	56.97	4.50	43.03
	#13	G62	1607.06	2.699	5.02	0.0031	28.70	1.92	71.30
	#14	D195	1054.13	7.478	9.29	0.0860	54.92	5.50	45.08
	#15	Z22-31	1248.26	4.934	5.97	0.0110	26.78	2.28	73.22
	#16	Q71	1437.20	2.351	4.78	0.0190	35.44	3.55	64.56

Table 2. Mineral content of 16 samples from the study area

Block	No	Mineral composition (wt.%)						Clay composition (wt.%)		
		Quartz	Feldspar	Carbonate	Pyrite	Anhydrite	Clay	Illite/Smectite	Illite	Chlorite
Heshui	#1	52.7	24.3	5.0	0.0	0.0	18.0	7.6	6.8	3.6
	#2	56.5	16.9	5.9	0.0	0.0	20.7	8.3	6.8	5.6
	#3	55.5	19.5	4.9	0.0	1.5	18.6	8.2	6.3	4.1
	#4	53.2	27	5.5	0.0	3.4	10.9	3.4	4.8	2.7
	#5	48.2	21.7	15.1	0.0	0.0	15.0	8.3	4.7	2
	#6	58.1	24.3	6.9	0.0	0.0	10.7	3.3	4.1	3.3
	#7	58.9	20.2	4.7	0.0	0.0	16.2	4.4	6.2	5.6
	#8	45.4	17.7	13.4	0.0	0.0	23.5	9.2	8.7	5.6
Ansai	#9	24.0	31.1	0.0	0.0	0.0	44.9	19.3	6.7	18.9
	#10	30.4	40.5	4.0	0.0	0.0	25.1	10.8	4.3	10.0
	#11	27.0	35.2	19.6	0.0	0.0	18.2	7.3	3.6	7.3
	#12	35.7	42.5	5.7	0.0	3.8	12.3	7.6	2.5	2.2
	#13	29.9	32.1	3.8	0.0	0.0	34.2	20.5	7.9	5.8
	#14	31.3	39.3	5.0	1.7	0.0	22.7	5.0	3.0	14.7
	#15	31.7	42.6	3.1	0.0	3.3	19.3	9.1	3.1	7.1
	#16	28.0	33.3	0.5	0.0	0.0	38.2	16.0	2.3	19.9

(mean 16.7%). There were few carbonate minerals. In the Ansai Block, quartz content was distributed between 24.0 and 35.7%, with average of 29.8%. Feldspar content ranged from 31.1 to 42.6% (average 37.1%). Clay content was relatively high, ranging from 12.3 to 44.9%, with average of 26.9%. Generally, the content of carbonate minerals in the Ansai Block was higher than in the Heshui Block. The clay minerals were primarily illite/smectite mixed layer, illite, and chlorite. In the Ansai Block, the main types of clay minerals were chlorite and

illite/smectite mixed layer, while those in the Heshui Block were illite and illite/smectite mixed layer.

EXPERIMENTAL METHODS AND PROCEDURES

NMR and Centrifugation

NMR is an effective technique for studying fluid occurrence in tight oil reservoirs (Li et al., 2019a; Wang & Zeng, 2020). The distribution characteristics of the T_2 spectrum are affected by fluid properties and rock pore structure, which can reflect a lot of physical information about rock. Long transverse relaxation time usually corresponds to a large pore-throat radius. Combined with centrifugal experiment, transverse relaxation time T_2 can also analyze quantitatively the movable fluid distribution in different pores according to the inverse relationship between pore size and relaxation rate of hydrogen nucleus (Al-Mahrooqi et al., 2006; Eslami et al., 2013).

NMR measurements were completed at the State Key Laboratory of Petroleum Resources and Prospecting, China University of Petroleum (Beijing). A Maran-drx/2 NMR instrument equipped with two pulsed gradient magnetic fields was used for core NMR measurement. The instrument has characteristics of fast test speed and good stability of repeated tests. The main working parameters of the instrument were as follows: test temperature 35 °C, number of echoes 8192, scanning times 128, working frequency 2 MHz, echo interval 0.1 ms, waiting time 6 s, gain 80%, and diameter of cylindrical core plugs 2.5 cm. The samples were saturated in simulated formation water (1.5% NaCl solution) with saturation pressure of 15 MPa for 36 h. The NMR experiments measured the T_2 spectrum under 100% water-saturated conditions. The samples are centrifuged at 21 psi,[1] 208 psi, and 417 psi for 1.5 h. The T_2 spectrum of the samples was measured after each centrifugation.

The appropriate centrifugal conditions were obtained by comparing the T_2 spectra for different centrifugal forces. Figure 2 shows a slight difference between T_2 spectra under centrifugal forces of 208 and 417 psi. Therefore, the residual fluid in the sample was considered the irreducible fluid after centrifugation at 417 psi. Additionally, according to the NMR test and centrifugation experiment, each sample's movable fluid porosity and saturation could be calculated (Table 1). Figure 3 shows the T_2 spectral distribution of samples with saturated water. The obvious differences in peak position, valley position, shape, and amplitude between T_2 spectra of samples confirmed the diversity of fluid occurrence characteristics in the Chang 7 sandstones. The T_2 spectra of the samples from the Ansai Block were characterized by unimodal, bimodal and trimodal distributions, while those from the Heshui Block were featured by unimodal and bimodal distributions. The T_2 cutoff value is an important parameter for analyzing fluid mobility, which can be affected by several factors, namely, lithology, fluid properties, pore structure (Testamanti & Rezaee, 2017; Yan et al., 2020; Zhao et al., 2021). The T_2 cutoff values of samples from the Heshui Block was distributed between 1.746 and 20.371 ms (mean 10.917 ms), while those for the Ansai Block ranged from 2.351 to 39.101 ms (average 8.277 ms) (Table 1).

HPMI

HPMI test is an important method for analyzing the pore structure of a tight oil reservoir (Loucks & Dutton, 2019; Zhang et al., 2019a). Previous studies have shown that the microscopic pore system of rock comprises an irregular capillary network (Al-Mahrooqi et al., 2006; Clarkson et al., 2012a, 2012b). According to the relationship between capillary pressure and pore-throat radius, the capillary pressure curve can be measured as:

$$P_c = \frac{2\sigma cos\theta}{r} \quad (1)$$

where σ is the interfacial tension (N/m) between the gas and mercury, P_c is the capillary force (MPa), θ is the wetting angle (°), and r is the pore-throat radius (μm). The shape of the capillary pressure curve is controlled by many factors, such as PSD and connectivity. Several parameters, such as median pressure, skewness, maximum pore-throat radius, sorting coefficient, and minimum mercury residual saturation, can be used to evaluate the micro-pore structure (Rezaee et al., 2012; Yao & Liu, 2012; Loucks & Dutton, 2019).

HPMI experiments were carried out on 16 samples from the study area (Fig. 4), and HPMI parameters are shown in Table 3. The inclined

[1] 1 psi = 6.89476 kPa.

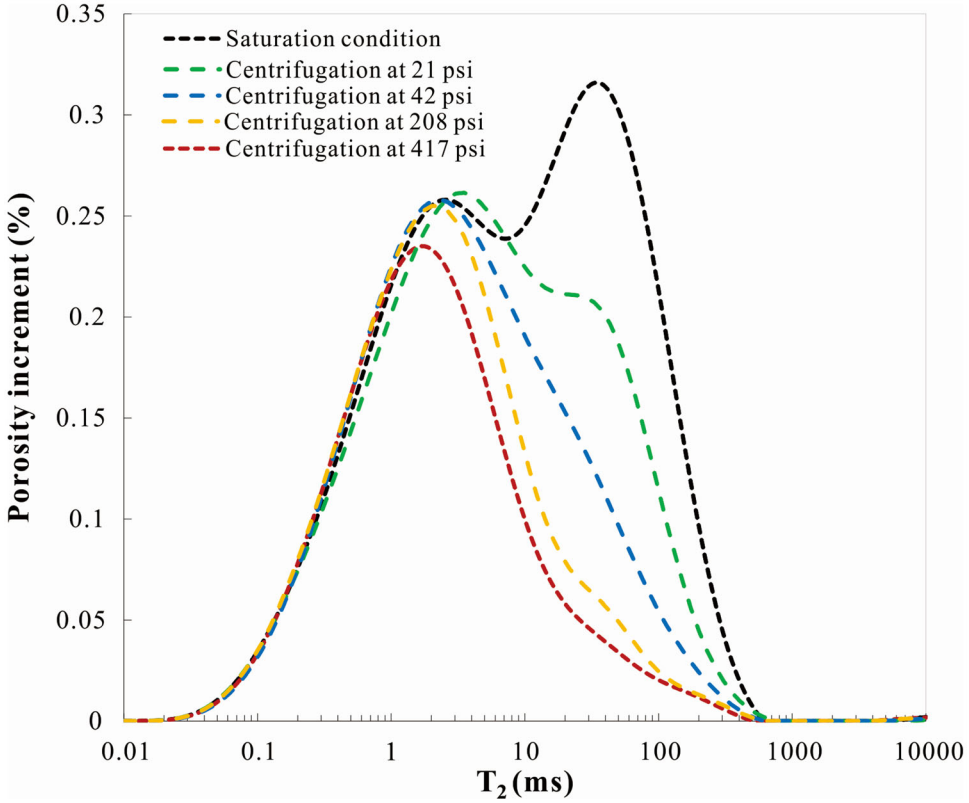

Figure 2. T_2 spectrum distribution for sample # 1 subjected to different centrifugal forces.

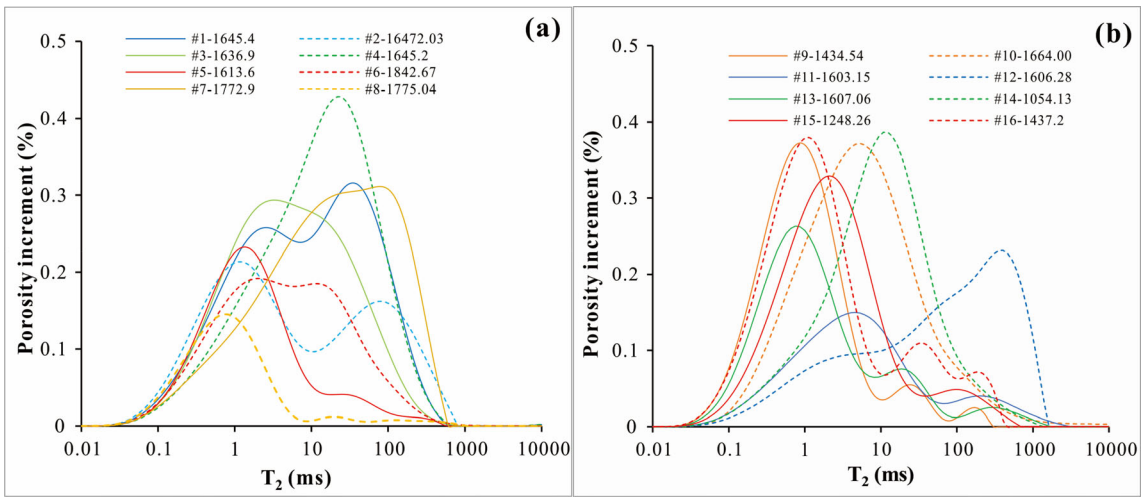

Figure 3. T_2 spectral distribution for samples with saturated water. (**a**) Heshui Block, (**b**) Ansai Block.

platform appears in most Heshui Block samples, while only in a few samples from the Ansai Block (Fig. 4). The curves for samples from the Heshui Block, compared to those from the Ansai Block, were positioned chiefly in the lower left of the coordinate axis. The displacement pressure (P_{cd}) of

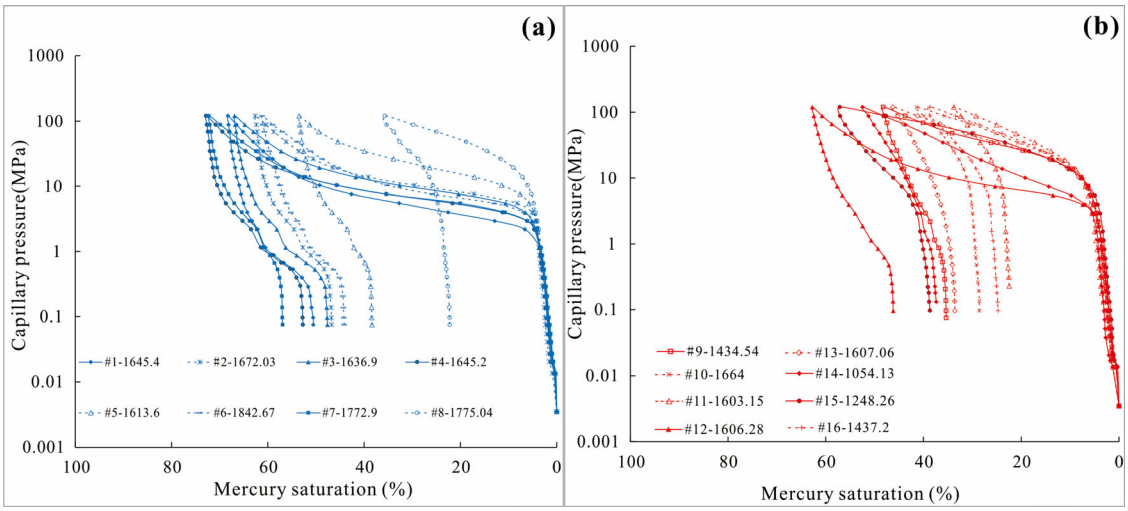

Figure 4. Capillary pressure curves for the Chang 7 sandstone samples. (**a**) Heshui Block. (**b**) Ansai Block.

Table 3. HPMI parameters of the Chang 7 sandstone samples in different areas

Area	No	Depth	R_{max} (μ m)	R_{ave} (μ m)	R_{50} (μm)	S_{max} (%)	P_{c50} (MPa)	P_{cd} (MPa)
Heshui	#1	1645.4	0.640	0.130	0.067	68.30	10.931	1.148
	#2	1672.03	0.185	0.059	0.029	62.62	25.100	3.983
	#3	1636.9	0.185	0.059	0.036	66.90	20.277	3.977
	#4	1645.2	0.250	0.081	0.059	72.84	12.515	2.939
	#5	1613.6	0.097	0.031	0.010	53.51	74.723	7.573
	#6	1842.67	0.249	0.075	0.024	61.20	30.496	2.947
	#7	1772.9	0.250	0.080	0.058	72.27	12.614	2.943
	#8	1775.04	0.071	0.017	–	35.72	–	10.323
Ansai	#9	1434.54	0.081	0.020	–	48.26	–	9.075
	#10	1664	0.095	0.019	–	41.41	–	7.768
	#11	1603.15	0.113	0.019	–	33.80	–	6.509
	#12	1606.28	0.436	0.072	0.029	62.76	25.160	1.685
	#13	1607.06	0.091	0.020	–	46.29	–	8.046
	#14	1054.13	0.300	0.022	0.007	52.50	104.890	2.454
	#15	1248.26	0.100	0.021	0.008	57.11	95.800	7.387
	#16	1437.2	0.054	0.016	–	42.47	–	10.074

R_{max} = maximum pore-throat radius (μm). R_{ave} = average pore-throat radius (μm). R_{50} = median pore-throat radius (μm). S_{max} = maximum mercury saturation (%). P_{c50} (MPa) = median pressure. P_{cd} = displacement pressure (MPa)

the Chang 7 sandstone samples ranged from 1.148 to 10.323 MPa (mean 5.552 MPa), and the corresponding maximum pore-throat radius (R_{max}) ranged between 0.054 and 0.640 μm (average 0.200 μm) (Table 3). The maximum mercury saturation (S_{max}) ranged from 33.80 to 72.84%, with average of 54.87%. The average pore-throat radius (R_{ave}) ranged between 0.016 and 0.130 μm (mean 0.046 μm). The R_{max}, R_{ave}, R_{50} and S_{max} of the samples from the Heshui Block were generally larger than those from the Ansai Block, while P_{c50} and P_{cd} of the samples from the Heshui Block were usually smaller than those from the Ansai Block. Generally, the pore structure of sandstone samples from the Ansai Block was generally more complex than those from the Heshui Block.

Casting Thin Sections and SEM

Casting thin section analysis can be used to identify qualitatively the pore structure characteristics of sandstone samples and to obtain information on the filler content and physical properties. Casting thin sections can be prepared by injecting the infusion fluids matched with oil-soluble dyes (red, blue) epoxy resin into the pores. The production process of casting thin sections follows the procedure for rock thin section preparation (SY/T 5913-2004). The final sample was polished with a thickness of 0.03 mm. SEM can be used to analyze pore distribution characteristics, authigenic mineral composition and characteristics, and other related information. Samples with appropriate sizes were selected for cutting, and a gold film was coated on its surface. Then, the sample was fixed on the observation table with conductive tape and placed in the observation chamber for analysis. The measurement of SEM was completed according to the general rules for measurement of length in microscale by SEM (GB/T 16594-2008).

RESULTS

Comparison of Reservoir Petrology Characteristics

The main types of sandstones in the Heshui Block were feldspar lithic fragment sandstone, while those in the Ansai Block were lithic fragment feldspar sandstone and feldspar sandstone (Fig. 5). Microscopic observation showed that the average quartz, feldspar and lithic fragments contents in the Heshui Block were 36.70%, 48.70%, and 14.60%, respectively. In contrast, the average quartz, feldspar, and lithic fragments contents in the Ansai Block were 42.9%, 45.53%, and 12.18%, respectively. XRD analysis showed that the average relative contents of illite, illite/smectite mixed layer, and chlorite in the Heshui Block were 38.85%, 37.46%, and 23.69%, respectively, while those in the Ansai Block were 14.92%, 49.18%, and 35.91%, respectively. Calcite and ankerite were the main carbonate minerals. There was a small amount of anhydrite and pyrite. The porosity of the Chang 7 sandstone was correlated positively with permeability (Fig. 6). The porosity of the samples from the Heshui Block was distributed primarily between 6.00 and 13.50%, with average of 9.17% (Fig. 6a). The permeability was chiefly distributed between 0.001 and 7.720×10^{-3} μm^2 (average 0.192×10^{-3} μm^2). The sandstone porosity from the Ansai Block was distributed mainly between 5.00 and 12.00% (mean 8.37%). However, the permeability was distributed chiefly 0.05 and 0.3×10^{-3}μm^2, with mean of 0.109×10^{-3} μm^2. Therefore, it can be concluded the Chang 7 reservoir in the study area is a typical tight oil reservoir. Microscopic observation showed that the sandstone clastic particles in the Heshui Block were mainly sub-angular, sub-circular, and moderately sorted, mainly in point and line contact. In contrast, the sandstone clastic particles in the Ansai Block were mostly sub-angular and well sorted, mainly in line contact.

Casting thin section analysis showed that the pore types of the Chang 7 sandstone were (1) inter-granular dissolution pores, (2) intra-granular dissolution pores, (3) residual inter-granular pores, (4) inter-crystalline pores, and (5) few micro-fractures (Fig. 7). Inter-granular dissolution pores usually appeared as irregular edges and mainly in the shape of a harbor, and longer dimensions generally ranged from 1.0 to 200.0 μm (Fig. 7a, b, c and d). The inter-granular dissolution pores in the Heshui Block were more developed than those in the Ansai Block. Intra-granular dissolution pores were distributed mainly in feldspar grains and often developed along cleavage (Fig. 7a, b, c, d and e). The longer dimensions of these pores were mainly between 0.5 and 150.0 μm. The residual pores were usually regular triangles or polygons (Fig. 7b and e). Many inter-crystalline pores were developed in the studied sandstone reservoirs (Fig. 7g, h and i). Such pores were usually developed on the walls of dissolution pores and residual inter-granular pores or particles' surfaces. The size of inter-crystalline pores was in the range of 10 nm–2.0 μm. The inter-crystalline pores in the Ansai Block were more developed than those in the Heshui Block. Few micro-fractures related to diagenesis and sedimentation exist in the Chang 7 sandstone (Fig. 7c). The throats were mainly flaky, curved, and tubular. In short, the Chang 7 sandstone in the Ansai and Heshui Blocks was characterized by small pores, thin throats, and poor reservoir connectivity.

Comparison of PSD Based on NMR Data

It is an effective method to convert T_2 spectrum into pore-throat radius distribution based on HPMI (Kleinberg, 1996; Huang et al., 2020; Wang & Zeng,

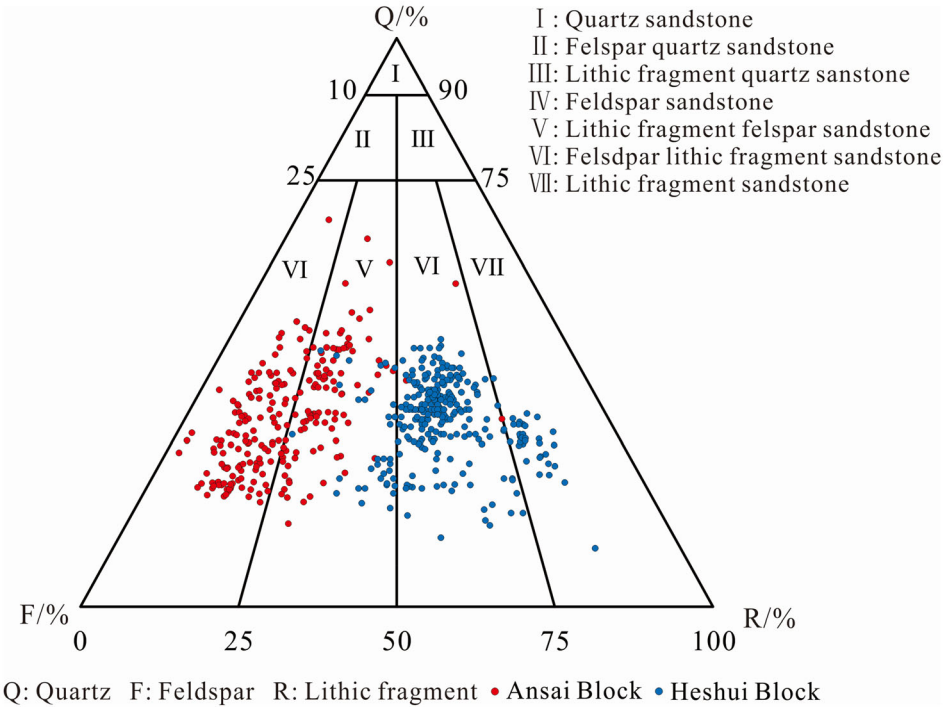

Figure 5. Classification of the lithology of the Chang 7 reservoir in the Ansai and Heshui Blocks.

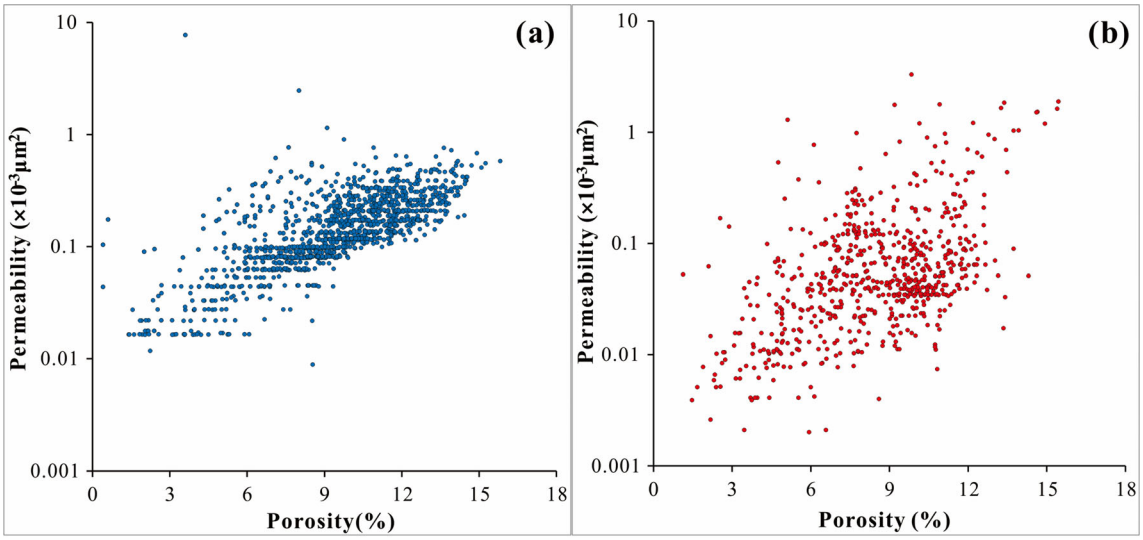

Figure 6. Relationship between porosity and permeability. (**a**) Heshui Block. (**b**) Ansai Block.

2020). It is a traditional method used to convert the T_2 spectrum into pore-throat radius distribution (Dunn et al., 2002), thus:

$$r_t = CT_2 \quad (2)$$

where r_t is the pore-throat radius (μm), and C is the conversion coefficient (μm/ms) related to the shape factor and the surface relaxation rate. However, a tight reservoir is characterized by complex micro/-

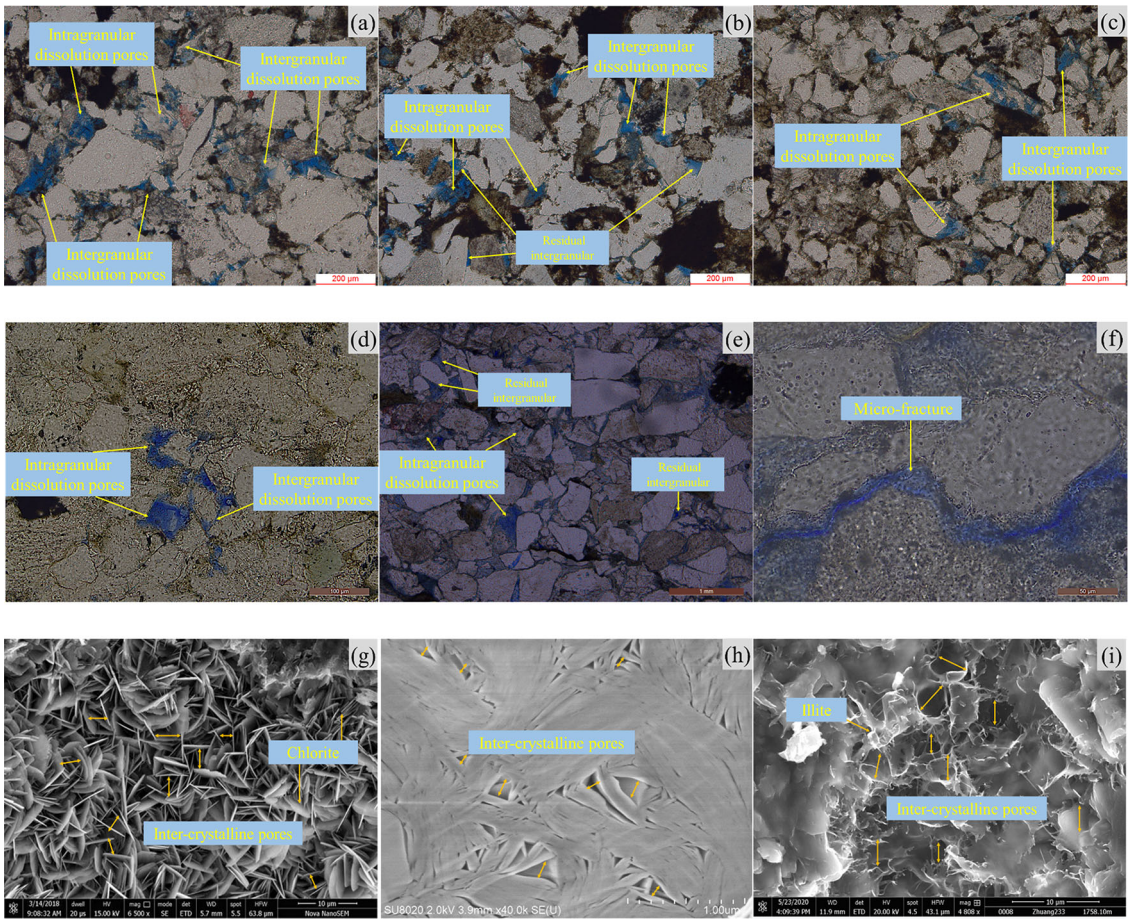

Figure 7. Pore systems of the Chang 7 tight oil reservoir. (**a**) Well L205, 1645.2 m, intra-granular dissolution pores and inter-granular dissolution pores (casting thin section) (Heshui Block). (**b**) Well Z225, 1772.9 m, intra-granular dissolution pores, inter-granular dissolution pores, and residual inter-granular (casting thin section) (Heshui Block). (**c**) Well L59, 1654.88 m, intra-granular dissolution pores and inter-granular dissolution pores (casting thin section) (Heshui Block). (**d**) Well Q129, 1666.88 m, inter-granular dissolution pores and intra-granular dissolution pores (casting thin section) (Ansai Block). (**e**) Well Z22-31, 1248.26 m, residual inter-granular and intra-granular dissolution pores (casting thin section) (Ansai Block). (**f**) Well Q168, 1664 m, micro-fracture (casting thin section) (Ansai Block). (**g**) Well D181, 1250.42 m, inter-crystalline pores (SEM) (Heshui Block). (**h**) Well Q129, 1669.76 m, inter-crystalline pores (SEM) (Ansai Block). (**i**) Well Z233, 1758.1 m, inter-crystalline pores (SEM) (Heshui Block).

nanoscale pore-throat structure, resulting in poor linear fit between T_2 and r_t. Therefore, based on Eq. 2, some experts and scholars have developed an empirical equation to convert accurately the transverse relaxation time T_2 to the pore-throat radius (Mao et al., 2005; Zhang et al., 2019a; Huang et al., 2020), thus:

$$r_t = CT_2^{1/n} \tag{3}$$

The pore-throat radius distribution curve constructed from the T_2 spectrum can be obtained by calculating the values of C and n. Pores of different scales correspond to different C and n values. Therefore, a ''3-stage'' construction method is proposed in this research to construct a large-scale pore-throat radius distribution accurately. The following is a brief explanation of the process.

At first, it is necessary to calculate the amplitude percentage of the T_2 spectrum according to NMR data, and then the accumulative amplitude percentage of T_2 and pore-throat radius are plotted (Fig. 8). When $S(i)$ (cumulative frequency) is less than S_{Hgmax} (maximum mercury saturation), $T_2(i)$ (transverse relaxation time) and $r_t(i)$ (pore-throat radius obtained by HPMI) have a one-to-one correspondence. $T_2(i)$ and $r_t(i)$ can be obtained by

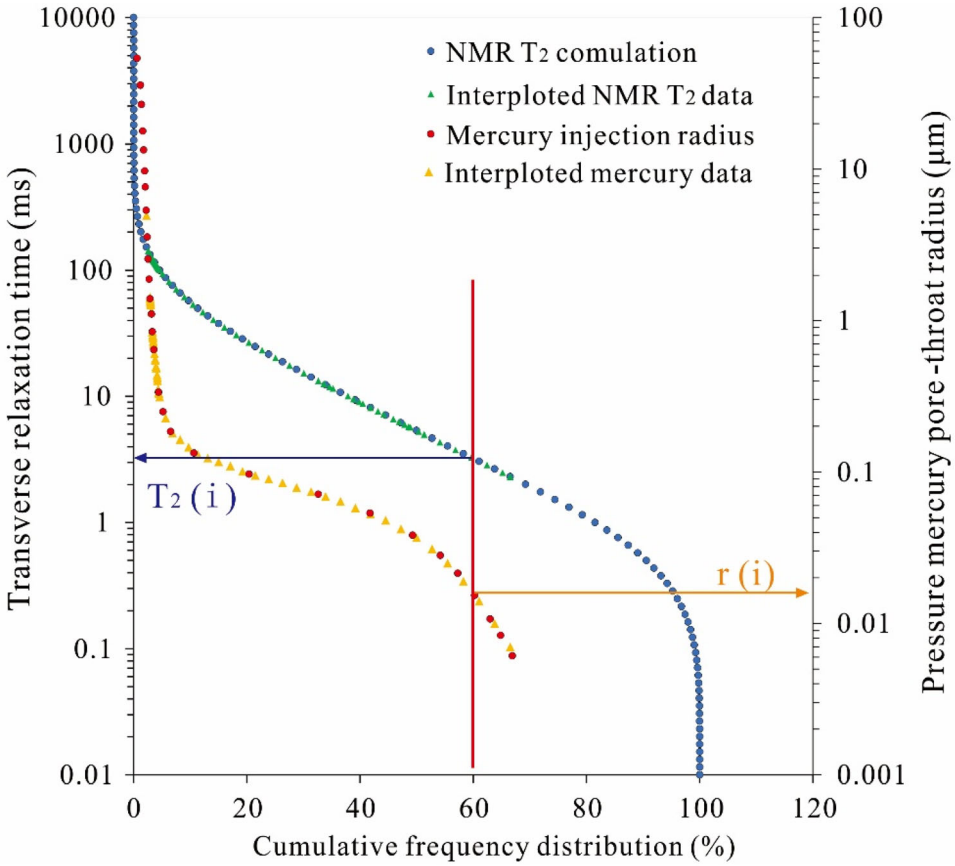

Figure 8. Conversion from transverse relaxation time T_2 to pore–throat radius.

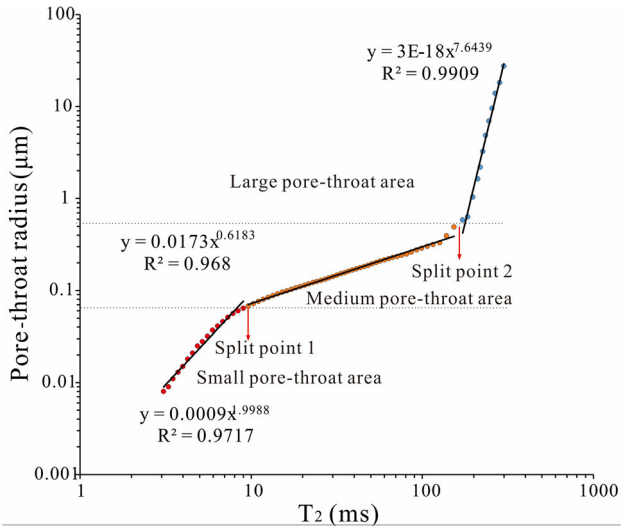

Figure 9. Fitting parameters of the conversion from NMR T_2 of Sample #1 to the pore-throat radius.

Table 4. Conversion factors between NMR T_2 spectrum and pore–throat radius and the corresponding correlation index

Block	No	Small pore-throat area			Split point 1 (μm)	Medium pore-throat area			Split point 2 (μm)	Large pore-throat area		
		C	n	R^2		C	n	R^2		C	n	R^2
Heshui Block	#1	0.0009	0.5003	0.9717	0.07	0.0173	1.6173	0.9921	0.54	3E−18	0.1308	0.9909
	#2	0.0029	0.6267	0.9626	0.04	0.0196	2.7442	0.9627	0.24	2E−26	0.0983	0.9710
	#3	0.0015	0.5117	0.9659	0.04	0.0180	1.9190	0.9924	019	2E−12	0.1758	0.9969
	#4	0.0002	0.4290	0.9919	0.03	0.0093	1.4424	0.9888	0.25	1E−14	0.1605	0.9995
	#5	0.0035	0.4278	0.9705	0.02	0.0179	1.8467	0.9821	0.15	2E−07	0.2829	0.992
	#6	0.0055	0.7171	0.9969	0.04	0.0206	2.0743	0.9938	0.18	8E−11	0.2066	0.9909
	#7	0.0003	0.5582	0.9833	0.06	0.0125	1.8839	0.9558	0.38	2E−27	0.0937	0.9988
	#8	0.0041	0.7284	0.9929	0.04	0.0289	3.9017	0.9485	0.08	6E−06	0.3866	0.9968
Ansai Block	#9	0.0074	0.7724	0.9650	0.04	0.0173	1.7873	0.9909	0.10	2E−05	0.3347	0.9626
	#10	0.0007	0.8941	0.9772	0.17	1E−11	0.2044	0.9999	21.94	1.18	1.7416	0.7442
	#11	0.0006	0.9769	0.9894	0.02	0.0025	1.7259	0.9537	0.08	2E−12	0.2226	0.9884
	#12	0.0002	0.7005	0.9849	0.05	0.0021	1.4802	0.973	0.24	9E−43	0.0712	0.9946
	#13	0.0044	0.7655	0.9898	0.02	0.0084	1.6750	0.9064	0.19	2E−07	0.3337	0.9504
	#14	0.00006	0.4930	0.9946	0.06	0.0025	1.0625	0.9955	0.40	4E−13	0.1766	0.9891
	#15	0.0036	1.0756	0.9851	0.05	0.0048	1.3633	0.9398	0.24	6E−11	0.2134	0.9793
	#16	0.0036	1.3193	0.9677	0.02	0.0019	1.1841	0.9763	0.13	8E−15	0.1556	0.9511

interpolating the r_t and T_2 cumulative frequency curves. Equation 3 can then be transformed into:

$$\ln r_t = \ln C + \frac{1}{n} \ln T_2 \tag{4}$$

Based on the principle of linear least squares, C and n can be acquired according to the fitting results of $T_2(i)$ and $r_t(i)$. Figure 9 shows that there are two inflection points at the pore-throat radius of about 0.54 and 0.07 μm. Therefore, the T_2 spectrum was divided into three sections to transform the distribution of pore-throat radius. Next, the C and n values of the 16 specimens were fitted (Table 4). Finally, the distribution of pore-throat radius transformed from the T_2 spectrum can be obtained by introducing C and n into Eq. 3. Figure 10 shows the comparison between the distribution of pore-throat radius transformed from the T_2 spectrum and obtained from HPMI. The two pore-throat radius distribution curves were highly consistent in shape and amplitude, showing that the ''3-stage'' calculation method was reasonable.

To evaluate the PSD characteristics accurately, the pores were divided into micron pores ($r > 1.0$ μm), submicron pores (0.1 μm $< r < 1.0$ μm), and nanoscale pores ($r < 0.1$ μm) according to the pore size converted from T_2 spectrum. The storage space of the Chang 7 sandstone was composed mainly of nanoscale pores, accounting for 58.10–94.60% of the total pores, with average of 84.70% (Table 5). The nanoscale pores content in the Heshui Block was lower than that in the Ansai Block. The average porosity value in the Heshui Block was 6.67%, while that in the Ansai Block was 7.65%. Submicron pores in the Chang 7 sandstone accounted for 2.67–39.81% of the total pores, with average of 12.84%. The submicron pores content in the Heshui Block was higher than in the Ansai Block. The average porosity in the Heshui Block was 2.09%, and that in the Ansai Block 0.55%. However, there were few micron pores in the Chang 7 sandstone.

Comparison of Fractal Characterizations Based on NMR Data

Fractal dimension can reflect the irregularity of pore structures. Previous studies showed the calculation model of fractal dimension based on NMR experimental data, which can be expressed as (Mandelbrot et al., 1984; Zhou et al., 2016a; Shao et al., 2017; Amadu & Pegg, 2018):

$$W = \left(\frac{T_2}{T_{2\max}}\right)^{3-D} \tag{5}$$

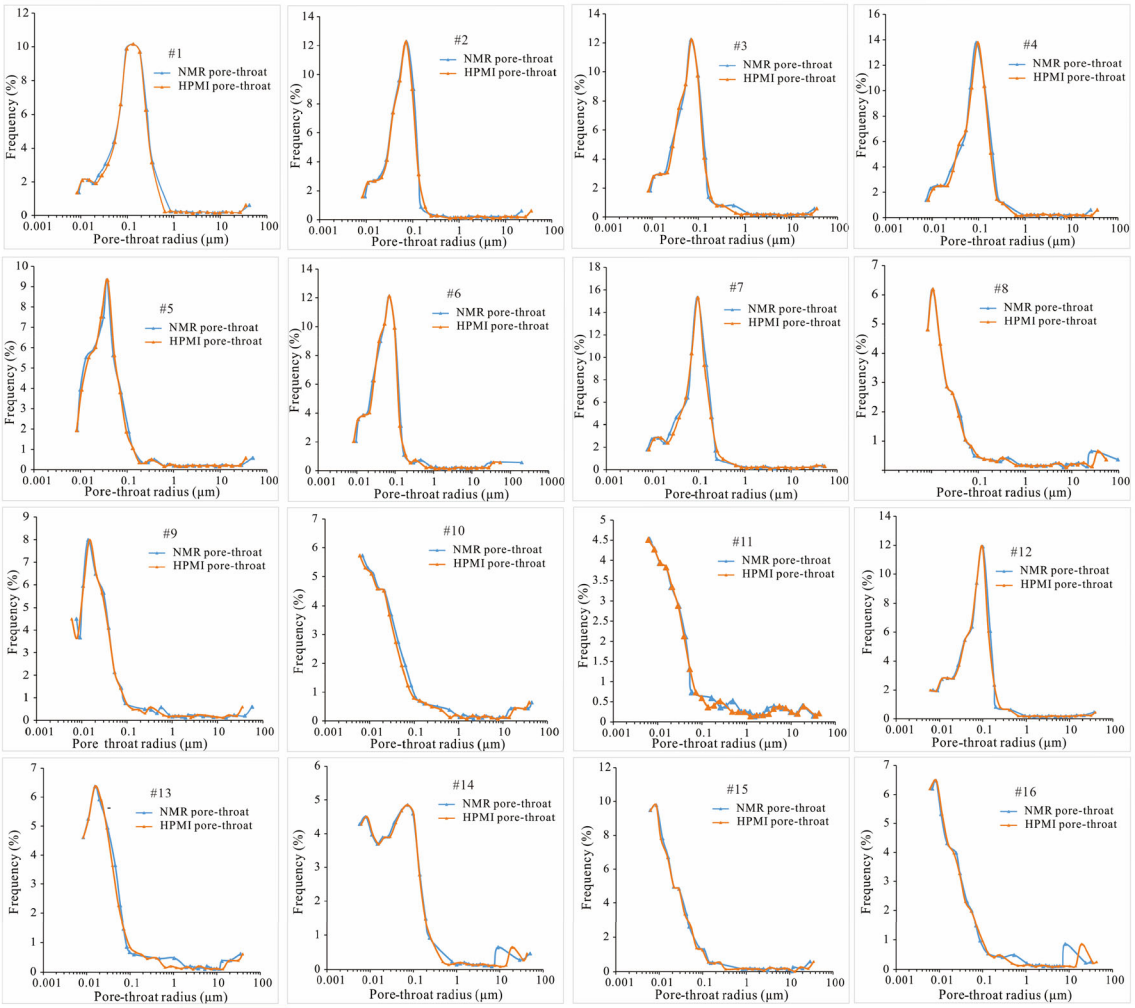

Figure 10. Comparison of pore-throat radius distribution of NMR and HPMI.

where D is the fractal dimension (unitless), T_2 is the transverse relaxation time (ms), W is the accumulative pore volume fraction (unitless), and $T_{2\ \max}$ is the maximum value of T_2 (ms). Equation 5 can be transformed as:

$$\log(W) = (3 - D)\log(T_2) + (D - 3)\log(T_{2\max}) \quad (6)$$

The straight-line slope (k) between log W and log T_2 can be obtained by introducing NMR experimental data into Eq. 6. Then, the fractal dimension D can be calculated.

Figure 11 shows the curve of log (W) vs. log (T_2). It can be divided into two segments at the positions of log ($T_{2\text{cutoff}}$). They have R^2 of greater than 0.85, which indicate that the Chang 7 sandstone can be characterized by fractal theory and has two sections of fractal structure. The fractal dimension D_{m} ($T_2 > T_{2\text{cutoff}}$), D_{b} ($T_2 < T_{2\text{cutoff}}$), and corresponding correlation coefficients are shown in Table 6. D_{m} is related to larger pores (movable fluid pores), and D_{b} is related to small pores (bound fluid pores) (Mao et al., 2005; Liu et al., 2018; Yang et al., 2020). The D_{m} and D_{b} are between 2.0 and 3.0, implying that fractal theory can be applied to describe movable fluid and bound fluid pores in the study area. This research mainly focuses on the occurrence characteristics of movable fluid. Therefore, only the fractal dimension (D_{m}) ($T_2 > T_{2\text{cutoff}}$)

Table 5. Petrophysical properties of the Chang 7 sandstone samples based on NMR

Area	No	NMR porosity (%)	Nanoscale pores		Submicron pores		Micron pores	
			Porosity, Φ_n (%)	Proportion, P_n (%)	Porosity, Φ_s (%)	Proportion, P_s (%)	Porosity, Φ_m (%)	Proportion, P_m (%)
Heshui Block	#1	11.83	6.87	58.10	4.71	39.81	0.25	2.10
	#2	8.55	7.12	83.31	1.24	14.51	0.19	2.18
	#3	10.58	8.54	80.78	1.80	16.99	0.24	2.24
	#4	12.64	8.42	66.61	3.98	31.47	0.24	1.92
	#5	5.49	5.12	93.18	0.24	4.44	0.13	2.38
	#6	7.45	6.48	86.98	0.87	11.68	0.10	1.34
	#7	11.88	7.90	66.51	3.83	32.23	0.15	1.25
	#8	3.08	2.92	94.60	0.08	2.67	0.08	2.74
Ansai Block	#9	8.26	7.77	94.03	0.25	3.03	0.24	2.93
	#10	11.23	10.46	93.19	0.41	3.65	0.36	3.16
	#11	4.90	4.56	93.09	0.18	3.58	0.16	3.33
	#12	7.90	6.11	77.38	1.59	20.14	0.20	2.48
	#13	6.68	6.20	92.83	0.27	4.01	0.21	3.16
	#14	10.01	8.8	87.92	0.89	8.88	0.32	3.2
	#15	8.52	7.97	93.55	0.37	4.33	0.18	2.12
	#16	10.02	9.33	93.13	0.40	3.96	0.29	2.84

Φ_n, Φ_s, and Φ_m denote porosity of nanoscale, submicron, and micron pores, respective. P_n, P_s, and P_m denote proportion of nanoscale, submicron, and micron pores, respectively

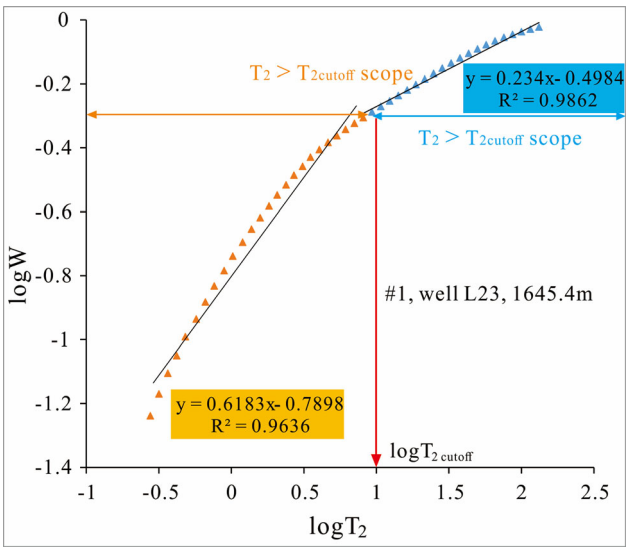

Figure 11. Fractal dimension curve of sample #1 from the Ansai Block based on NMR data.

was used to study the movable fluids occurrence. The R^2 of the linear fitting curves was distributed mainly between 0.8578 and 0.9981, showing good correlation. The D_m in the Heshui Block ranged from 2.7318 to 2.9681 (mean 2.8303), and that in the Ansai Block ranged from 2.7318 to 2.9445 (average 2.8553). Thus, the PSH in the Ansai Block was slightly stronger than that in the Heshui Block.

Table 6. Fractal dimensions of tight sandstone samples based on NMR data

Heshui Block					Ansai Block				
Sample No	$T_2 > T_{2cutoff}$		$T_2 < T_{2cutoff}$		Sample No	$T_2 > T_{2cutoff}$		$T_2 < T_{2cutoff}$	
	Fractal dimension (D_m)	R^2	Fractal dimension (D_b)	R^2		Fractal dimension (D_m)	R^2	Fractal dimension (D_b)	R^2
#1	2.7660	0.9862	2.3817	0.9636	#9	2.9445	0.9319	2.1476	0.9481
#2	2.8430	0.9981	2.4581	0.9981	#10	2.7904	0.9131	2.1595	0.9823
#3	2.7962	0.9683	2.2499	0.9687	#11	2.8723	0.8578	2.213	0.9827
#4	2.7381	0.9614	2.2398	0.9867	#12	2.7318	0.9972	2.5518	0.9678
#5	2.8781	0.8664	2.0202	0.9806	#13	2.9131	0.9872	2.1565	0.9419
#6	2.8969	0.9564	2.4600	0.9335	#14	2.7477	0.9168	2.2591	0.997
#7	2.7564	0.9891	2.4263	0.9869	#15	2.9267	0.8819	2.1865	0.9661
#8	2.9681	0.9359	2.1219	0.9516	#16	2.9165	0.9723	2.1359	0.9669

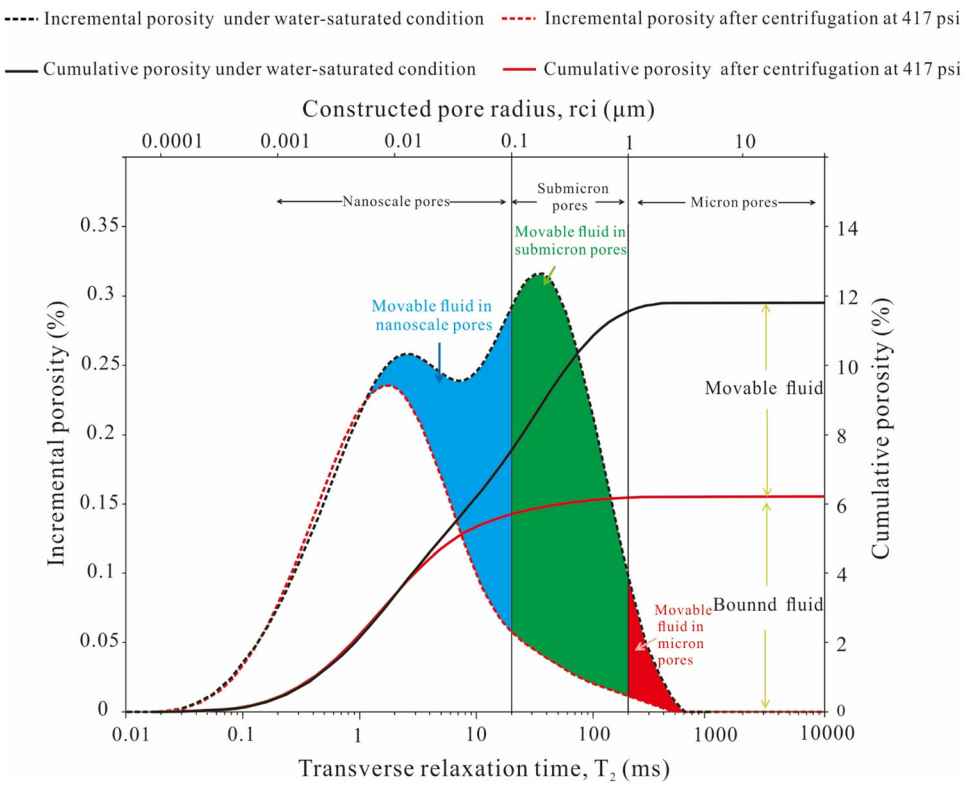

Figure 12. Model diagram of movable fluid distribution in different pores of sample #1.

Comparison of Movable Fluid Distribution

The Chang 7 sandstone showed a wide range of movable fluid saturation (S_m) ranging from 17.03 to 56.97%, with average of 40.81% (Table 1). The movable fluid porosity (Φ_m) was distributed between 0.53 and 6.20%, with mean of 3.69%. The movable fluid content in the Heshui Block was slightly higher than that in the Ansai Block. The distribution of Φ_m in the Heshui Block was chiefly between 0.53 and 6.20% (average 3.92%), while S_m ranged from 17.03 to 49.03%, with mean of 40.97%. In contrast, the

Table 7. Movable fluid distribution parameters of the Chang 7 sandstone samples

Area	Sample No	Movable fluid in different pores								
		Nanoscale pores			Submicron pores			Micron pores		
		Porosity, Φ_{mn} (%)	Saturation S_{m1} (%)	Proportion, P_{mn} (%)	Porosity, Φ_{ms} (%)	Saturation, S_{m2} (%)	Proportion, P_{ms} (%)	Porosity, Φ_{mm} (%)	Saturation, S_{m2} (%)	Proportion, P_{mm} (%)
Heshui	#1	1.33	11.20	23.65	4.07	34.40	72.59	0.21	1.78	3.76
	#2	2.22	25.92	66.04	0.99	11.55	29.41	0.15	1.79	4.55
	#3	2.90	27.44	62.14	1.61	15.25	34.52	0.16	1.48	3.36
	#4	2.30	18.22	37.17	3.71	29.38	59.93	0.18	1.43	2.91
	#5	2.09	38.03	89.47	0.17	3.16	7.44	0.07	1.31	3.09
	#6	2.31	31.39	77.22	0.64	8.65	21.27	0.05	0.62	1.53
	#7	2.13	17.97	37.64	3.43	28.87	60.50	0.11	0.89	1.86
	#8	0.49	15.91	93.40	0.01	0.45	2.65	0.02	0.69	4.03
Ansai	#9	1.26	15.26	83.90	0.13	1.63	8.97	0.11	1.30	7.13
	#10	5.14	45.78	88.58	0.35	3.15	6.09	0.31	2.75	5.33
	#11	2.25	45.99	87.69	0.16	3.34	6.38	0.15	3.11	5.93
	#12	2.78	35.17	61.74	1.53	19.31	33.90	0.20	2.48	4.36
	#13	1.63	24.41	85.06	0.13	1.88	6.56	0.16	2.40	8.36
	#14	4.46	44.58	81.19	0.79	7.86	14.32	0.25	2.47	4.49
	#15	1.91	22.44	83.79	0.24	2.84	10.62	0.13	1.50	5.61
	#16	2.93	29.23	82.49	0.36	3.55	10.02	0.27	2.65	7.49

Φ_{mn}, Φ_{ms}, and Φ_{mm} denote movable fluid porosity in nanoscale, submicron, and micron pores, respectively. S_{m1}, S_{m2}, and S_{m3} denote movable fluid saturation in nanoscale, submicron, and micron pores, respectively. P_{mn}, P_{ms}, and P_{mm} denote movable fluid proportion in nanoscale, submicron, and micron pores, respectively

distribution of Φ_m in the Ansai Block was between 1.51 and 5.80% (mean 3.45%), whereas S_m mainly ranged from 18.21 to 56.97%, with average of 40.64%.

The amplitude of T_2 spectra can reflect the volume of different pores and the fluid content in different pores. The difference between the amplitude of T_2 spectra under a water-saturated state and after centrifugation at 417 psi can reflect the movable fluid distribution in different pores. Using sample # 1 as an example, according to Eq. 3 and Table 4, the movable fluid content in different pores was obtained (Fig. 12). The movable fluid distribution parameters of the studied samples are shown in Table 7. The movable fluids of the Chang 7 sandstone are distributed mainly in nanoscale pores, followed by submicron pores. Movable fluid proportion in nanoscale pores (P_{mn}) was 23.65–93.40% (mean 71.32%), while in submicron pores (P_{ms}) it ranged from 2.65 to 72.59% (average 24.07%). Movable fluid porosity in nanoscale pores (Φ_{mn}) was distributed between 0.49 and 5.14% (average 2.38%), whereas in submicron pores (Φ_{ms}) it ranged from 0.01 to 4.07%, with mean of 1.15%. Movable fluid saturation in nanoscale pores (S_{mn}) ranged from 11.20 to 45.99%, with mean of 28.06%, whereas submicron pores (S_{ms}) were distributed between 0.45 and 34.40%, with average of 10.95%. A small amount of movable fluid was distributed in the micron pores of the Chang 7 sandstone.

The movable fluid content in the nanoscale pores in the Ansai Block was higher than that in the Heshui Block. The average Φ_{mn} in the Heshui Block was 1.97%, whereas in the Ansai Block it was 2.80%. The average P_{mn} in the Heshui Block was 60.75%, while in the Ansai Block it was 81.81%. The movable fluid content in the submicron pores in the Ansai Block was lower than that in the Heshui Block. Similarly, the average Φ_{ms} in the Heshui Block was 1.84%, whereas in the Ansai Block it was 0.46%. The average S_{ms} in the Heshui Block was 16.69%; however, the average S_{ms} in the Ansai Block was 5.45%. The average P_{ms} in the Heshui Block was 36.40%, while in the Ansai Block it was 12.11%.

DISCUSSION

Relationship between Physical Properties and Movable Fluid

Figure 13 shows that reservoirs with good physical properties usually have high movable fluid content. Generally, the S_m of the studied samples was correlated positively with physical properties. However, in some of the samples, the S_m decreased with increase in porosity and permeability. These characteristics show that a single factor does not control movable fluid distribution. The relationship

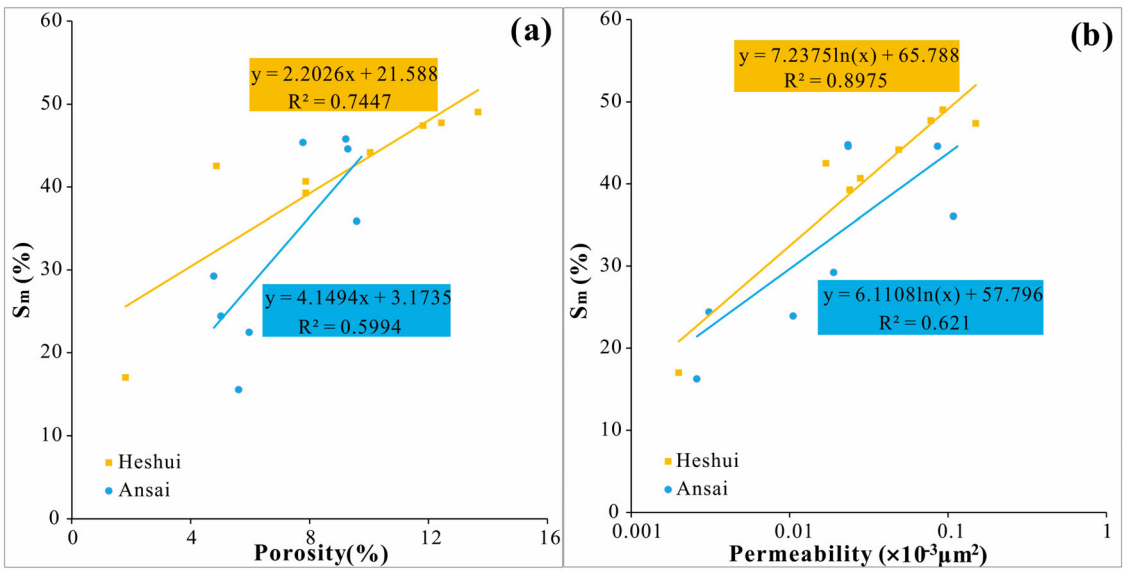

Figure 13. Relationship of movable fluid saturation S_m with (**a**) porosity and (**b**) permeability.

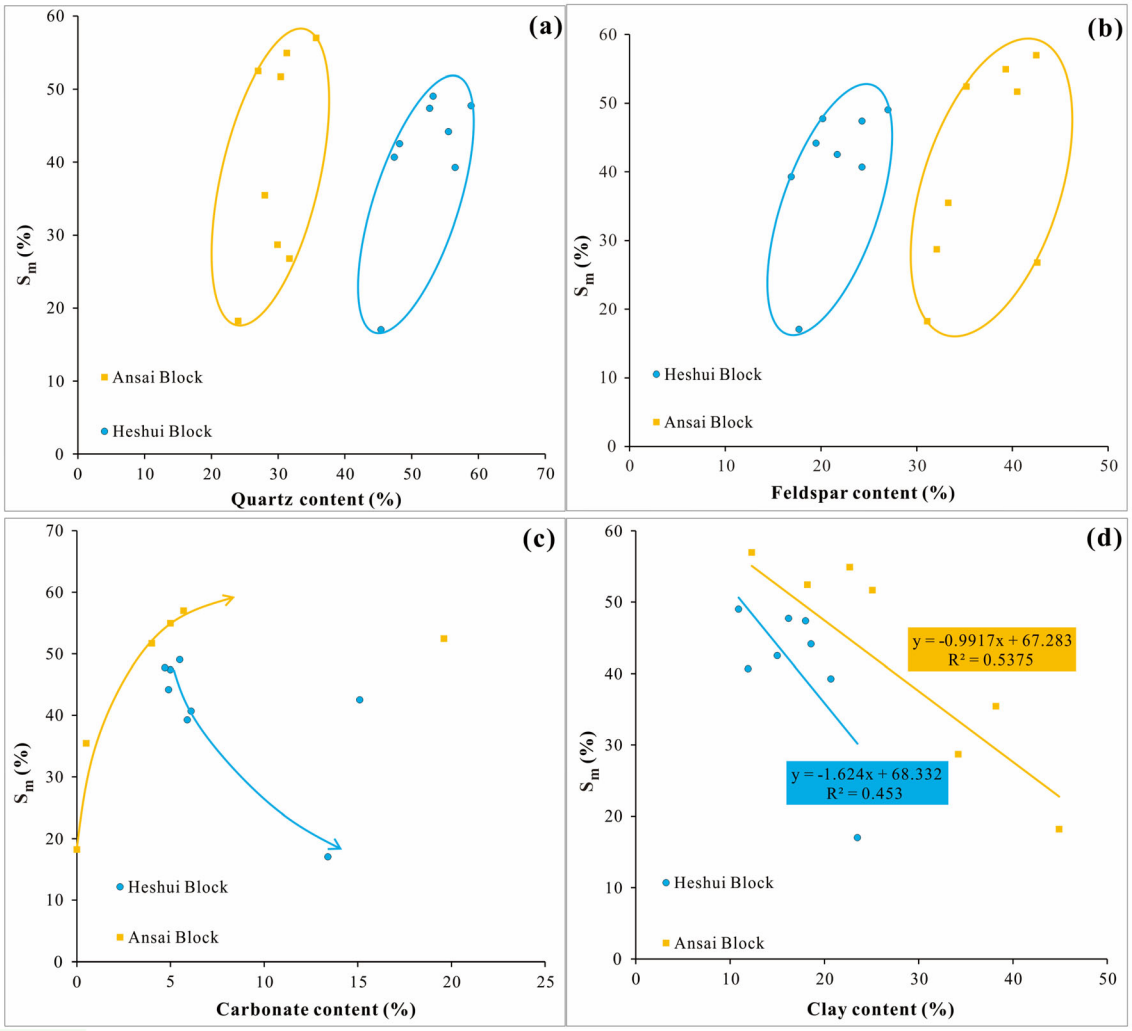

Figure 14. Scatter plots of movable fluid saturation S_m vs. contents of (**a**) quartz, (**b**) feldspar, (**c**) carbonate minerals, and (**d**) clay minerals.

of S_m with porosity and permeability in the Ansai Block is weaker than that in the Heshui Block. This may be due to the more complex occurrence mechanism of movable fluid in the Ansai Block. The permeability reflected the percolation capacity of the reservoir, and the porosity reflected the reservoir's storage capacity (Rosenbrand et al., 2015; Lai et al., 2018b; Liu et al., 2020b). The S_m was more closely related to permeability than porosity, indicating percolation capacity of the reservoir had a more significant influence on movable fluid occurrence.

Influence of Mineral Composition on Movable Fluid

Previous studies revealed that brittle framework mineral grains increase the resistance to overburden pressure, which is helpful for the preservation of residual inter-granular pores (Ajdukiewicz & Larese, 2012; Qiao et al., 2020c; Yang et al., 2020). However, ductile clastic minerals are susceptible to compaction, which is not conducive to the preservation of residual inter-granular pores (Mao et al., 2020). Figure 14 shows that the difference in rock mineral composition affects the movable fluid content, and the relationship between

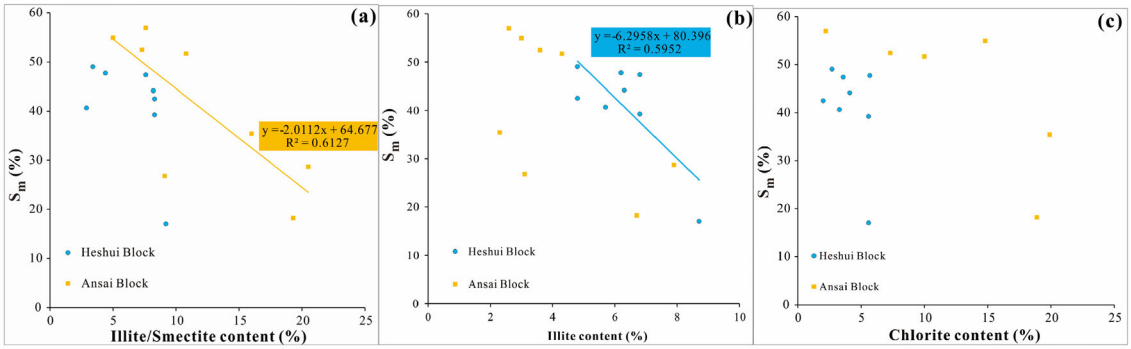

Figure 15. Correlation of the movable fluid saturation S_m vs. the contents of illite/smectite (**a**), illite (**b**), and chlorite (**c**).

mineral composition and movable fluid content varies with mineral type. High quartz content provides adequate conditions for the preservation of residual inter-granular pores and it improves the connectivity of pores, resulting in positive correlation between quartz content and S_m (Fig. 14a). Feldspar dissolution produces dissolution pores, which also provide a source for the precipitation of clay minerals, leading to simultaneous precipitation of clay minerals blocking pore space (Qiao et al., 2020c; Yang et al., 2020; Yin et al., 2020; Liu et al., 2021). Therefore, there was a weak positive correlation between feldspar and movable fluid content (Fig. 14b). Carbonate cementation can destroy a reservoir's pore structure and decrease the pore connectivity network. However, the dissolution of early carbonate cement can improve pore network connectivity. Figure 14c shows the influence of carbonate on pore connectivity, which is more obvious in the carbonate dissolution in the Ansai Block, resulting in weak positive relationship between S_m and carbonate content. However, the influence of carbonate dissolution on pore connectivity is more obvious than carbonate cementation in the Heshui Block, resulting in weak negative correlation between S_m and carbonate content. Clay minerals have dual effects on pore connectivity, which depends on the types and forms of clay minerals (Liu et al., 2021). Clay minerals in pores generally occlude throats and obstruct the connection of pores. However, clay minerals wrapped on particle surfaces can enhance the anti-compaction ability and inhibit the overgrowth of quartz, which is beneficial to pore connectivity (Ajdukiewicz & Larese, 2012). Figure 14d shows that the destruction of clay minerals on pore connectivity was more significant, thus reducing movable fluid content.

Figure 15 shows that different types of clay have a diverse effect on movable fluid content. The relationship between illite/smectite mixing layer and movable fluid content in the Ansai Block was closer than that in the Heshui Block (Fig. 15a). The influence of illite on movable fluid content in the Ansai Block was more obvious than in the Heshui Block (Fig. 15b). The correlation between S_m and chlorite content was very poor (Fig. 15c), which was caused by the influence of chlorite on pore connectivity varying with the occurrence form. Chlorite in intergranular pore can complicate pore structure and hinder pore connectivity (Mao et al., 2020). However, chlorite wrapped on particle surfaces can enhance the anti-compaction ability and inhibit the overgrowth of quartz, which is conducive to improving pore connectivity.

Influence of Pore Size and Distribution on Movable Fluid

NMR porosity is a parameter characterizing the total pore space of a reservoir. Figure 16a shows that reservoirs with large NMR porosity usually correspond to higher movable fluid content. The correlation coefficient R^2 between NMR porosity and Φ_m in the Heshui Block was larger than that in the Ansai Block, indicating that the influence of total pore space on movable fluid content in the Heshui Block was more significant than in the Ansai Block.

The effects of different pores on the movable fluid occurrence were various (Fig. 16b, c and d). The nanoscale pores were not conducive to the accumulation of movable fluid due to their poor connectivity (Fig. 16b). The average nanoscale pore porosity was 7.16%, whereas the average movable

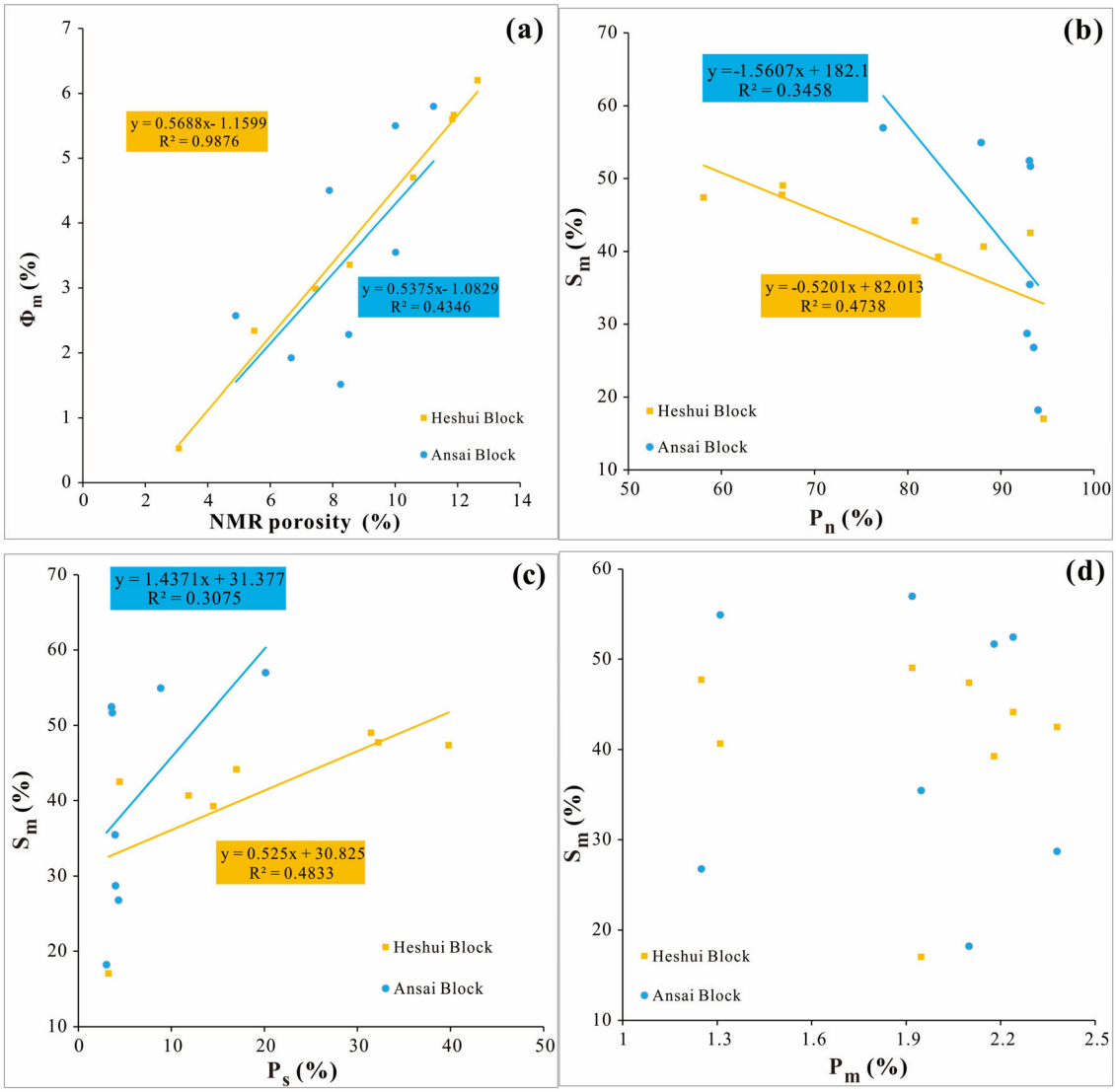

Figure 16. Correlation of NMR porosity and PSD parameters from NMR with movable fluid porosity Φ_m. Movable fluid saturation S_m vs. (**a**) NMR porosity, (**b**) nanoscale pore proportion P_n, (**c**) submicron pore proportion P_s, and (**d**) submicron pore proportion P_m.

fluid porosity in nanoscale pores was 2.38% (Tables 5 and 7). This revealed the most nanoscale pores were invalid. Therefore, sandstone reservoirs with more nanoscale pores usually have poor connectivity and strong heterogeneity, leading to low movable fluid content. The relatively good connectivity of submicron pores was beneficial to the accumulation of movable fluids. Therefore, Chang 7 sandstone reservoirs with more submicron pores usually have weak heterogeneity and good pore connectivity, resulting in high movable fluid content (Fig. 16c). With increase in nanoscale and submicron pores, the change of movable fluid saturation in the Ansai Block was faster than that in the Heshui Block (Fig. 16b and c). It can be inferred that the movable fluid content in the Ansai Block was more sensitive to PSD than that in the Heshui Block. Figure 16d shows that micron pores have no apparent effect on movable fluid content due to the small number of micron pores in the Chang 7 sandstone reservoir. Although micron pores are not the main contributor to storage space in tight oil reservoirs and the primary storage space of movable

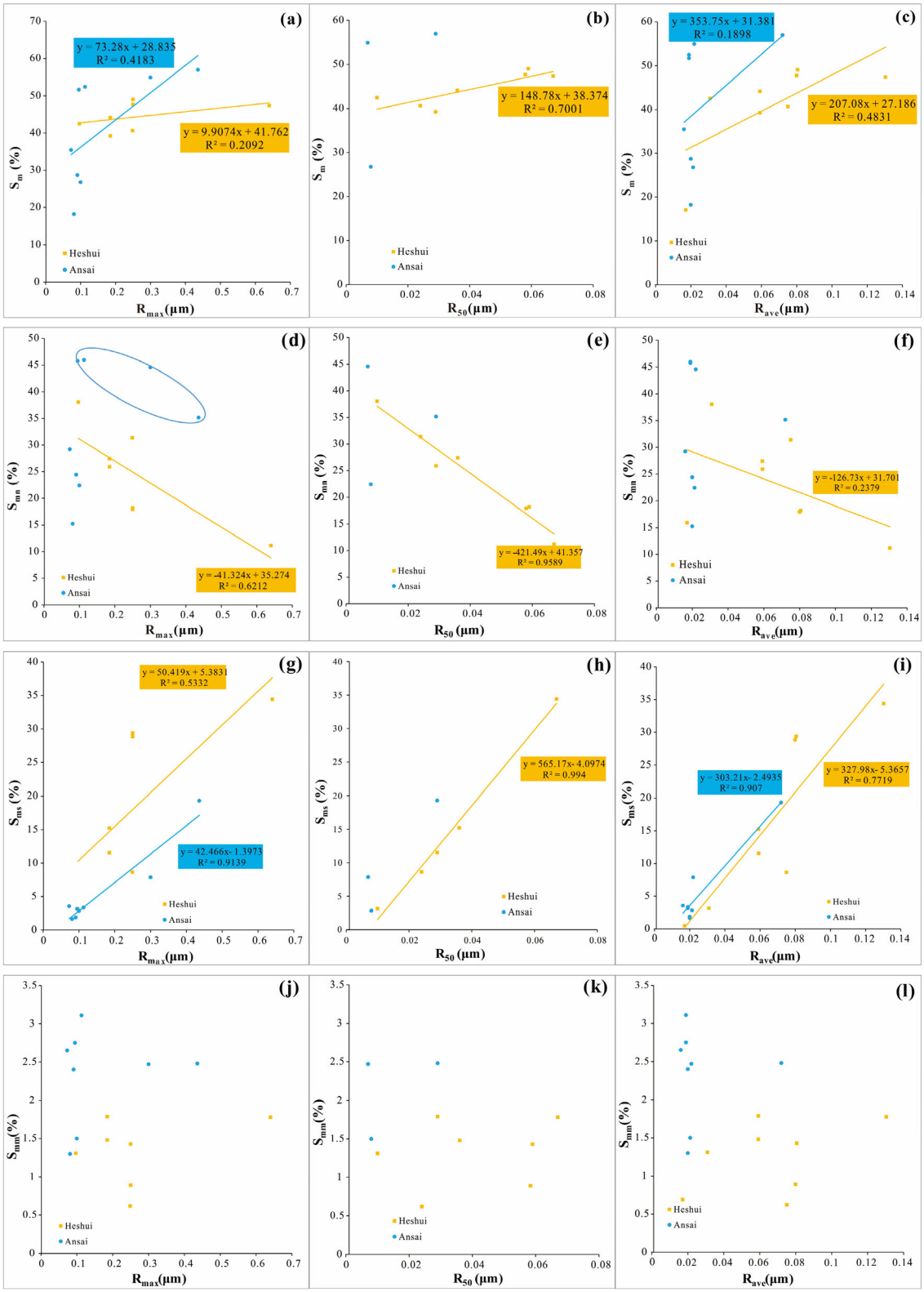
(a)
y = 73.28x + 28.835
R² = 0.4183
y = 9.9074x + 41.762
R² = 0.2092
Heshui
Ansai
Sm (%)
Rmax(μm)
(b)
y = 148.78x + 38.374
R² = 0.7001
Heshui
Ansai
Sm (%)
R50(μm)
(c)
y = 353.75x + 31.381
R² = 0.1898
y = 207.08x + 27.186
R² = 0.4831
Heshui
Ansai
Sm (%)
Rave(μm)
(d)
y = -41.324x + 35.274
R² = 0.6212
Heshui
Ansai
Smn (%)
Rmax(μm)
(e)
y = -421.49x + 41.357
R² = 0.9589
Heshui
Ansai
Smn (%)
R50 (μm)
(f)
y = -126.73x + 31.701
R² = 0.2379
Heshui
Ansai
Smn (%)
Rave(μm)
(g)
y = 50.419x + 5.3831
R² = 0.5332
y = 42.466x - 1.3973
R² = 0.9139
Heshui
Ansai
Sms (%)
Rmax(μm)
(h)
y = 565.17x - 4.0974
R² = 0.994
Heshui
Ansai
Sms (%)
R50 (μm)
(i)
y = 303.21x - 2.4935
R² = 0.907
y = 327.98x - 5.3657
R² = 0.7719
Heshui
Ansai
Sms(%)
Rave(μm)
(j)
Heshui
Ansai
Smm(%)
Rmax(μm)
(k)
Heshui
Ansai
Smm(%)
R50 (μm)
(l)
Heshui
Ansai
Smm(%)
Rave(μm)

◀**Figure 17.** Relationships between movable fluid distribution parameters and pore size parameters. Movable fluid saturation S_m vs. (**a**) maximum pore-throat radius R_{max}, (**b**) median pore-throat radius R_{50}, and (**c**) average pore-throat radius R_{ave}. Movable fluid saturation in nanoscale pores S_{mn} vs. (**d**) R_{max}, (**e**) R_{50}, and (**f**) R_{ave}. Movable fluid saturation in submicron pores S_{mn} vs. (**g**) R_{max}, (**h**) R_{50}, and (**i**) R_{ave}. Movable fluid saturation in micron pores S_{mn} vs. (**j**) R_{max}, (**k**) R_{50}, and (**l**) R_{ave}.

fluid, their development can significantly increase the percolation capacity of reservoirs.

The correlations between the S_m and pore size parameters varied in different areas (Fig. 17a, b and c). There were few R_{50} values in the Ansai Block, and so the influence of R_{50} on the movable fluid content in the Ansai Block is not discussed here. The relationship between R_{max} and S_m in the Heshui Block was better than that in the Ansai Block, while the relationship between R_{ave} and S_m in the Ansai Block was better than that in the Heshui Block (Fig. 17a and c). These results show that the influence of pore size on movable fluid content in different areas is diverse. In contrast, S_m was more closely related to R_{50} than to R_{max} and R_{ave} in the Heshui Block, indicating that R_{50} can better reflect movable fluid content in a tight sandstone reservoir (Fig. 17b). The influence of pore size parameters on movable fluid in different pores was diverse (Fig. 17d, e, f, g, h, i, j, k and l). Reservoirs with large R_{max} and R_{ave} were not conducive to the accumulation of movable fluid in the nanoscale pores in the Heshui Block (Fig. 17d and f). When R_{max} was greater than 0.10 μm, S_{mn} tended to decrease with increase in R_{max} in the Ansai Block (Fig. 17d), while R_{ave} had no significant impact on S_{mn} (Fig. 17f). Reservoirs with large R_{max} and R_{ave} generally corresponded to high content movable fluid in submicron pores (Fig. 17g and i). In the Heshui Block, reservoirs with large R_{50} were conducive to movable fluid occurrence in submicron pores, but not in nanoscale pores (Fig. 17e and h). The S_{mn} had no obvious relationship with R_{max}, R_{ave}, and R_{50}, which may be due to the low movable fluid content in micron pores (Fig. 17j, k and l).

Influence of Heterogeneity on Movable Fluid

The D_m is correlated negatively with the S_m and Φ_m, indicating that fractal characteristics are an important factor affecting movable fluid distribution in the tight sandstone (Fig. 18). The Chang 7 sandstone reservoir with strong heterogeneity corresponds generally to low movable fluid content, leaving less oil and gas to exist in this kind of reservoir. However, the Chang 7 sandstone reservoir with weak heterogeneity corresponds usually to high movable fluid content, which is favorable for oil and gas enrichment.

The influence of heterogeneity on movable fluid in different pores in the study areas varied (Fig. 19). The correlation coefficient (R^2) between Φ_{mn} and D_m in the Ansai Block was larger compared to that in the Heshui Block, and the linear slope was gentler (Fig. 19a). This shows that the influence of heterogeneity on movable fluid in the nanoscale pores in the Ansai Block was stronger than in the Heshui Block. In contrast, the R^2 between D_m vs. Φ_{ms} in the Heshui Block was larger, and the linear slope was gentler (Fig. 19b). This shows that the influence of heterogeneity on movable fluid in submicron pores in the Heshui Block was stronger than in the Ansai Block. Figure 19a, b, d and e show that heterogeneity had a more substantial impact on movable fluid in submicron pores in the Heshui Block than nanoscale pores. In contrast, it had a stronger impact on movable fluid in the Ansai Block nanoscale pores than submicron pores. A small amount of movable fluid was distributed in micron pores, leading to the small slope of the fitting curve between Φ_{ms} and D_m (Fig. 19c). In the Heshui Block, the sensitivity of movable fluid content in submicron pores to heterogeneity was stronger than in nanoscale pores, resulting in positive correlation between Φ_{mn} and D_m (Fig. 19d). Generally, in the Ansai Block, the inhibition of strong heterogeneity on movable fluid occurrence in nanoscale pores was stronger than in submicron pores. However, in the Heshui Block, the inhibition of strong heterogeneity on the accumulation of movable fluid in submicron pores was stronger than in nanoscale pores. Strong heterogeneity did not significantly inhibit the accumulation of movable fluid in micron pores.

CONCLUSIONS

This paper discussed the comparison of PSD, heterogeneity, and occurrence characteristics of movable fluids of tight oil reservoirs formed in different sedimentary environments by means of nuclear magnetic resonance, high-pressure mercury

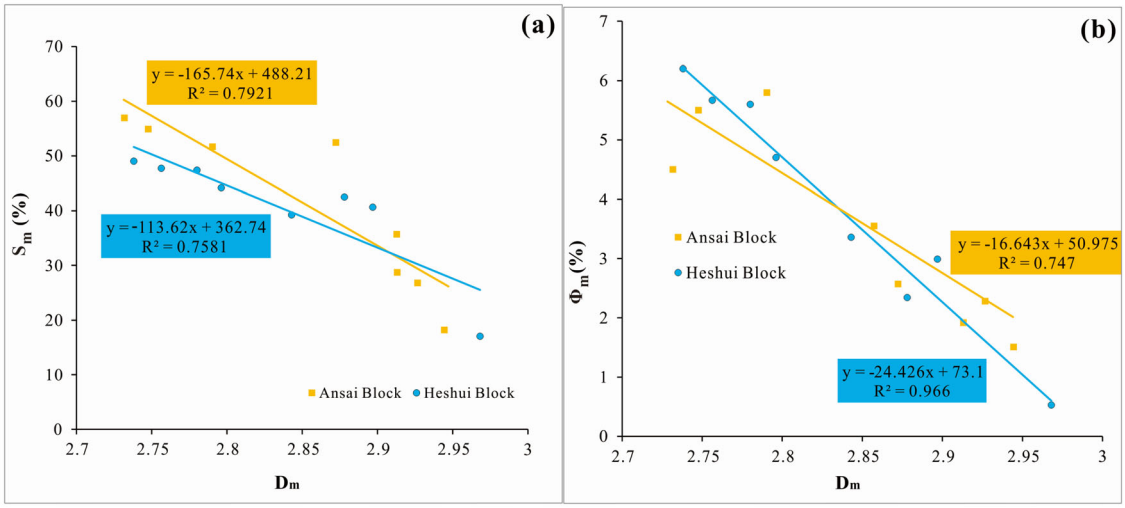

Fig. 18. Relationships of fractal dimension D_m vs. (**a**) movable fluid saturation S_m and (**b**) movable fluid porosity Φ_m.

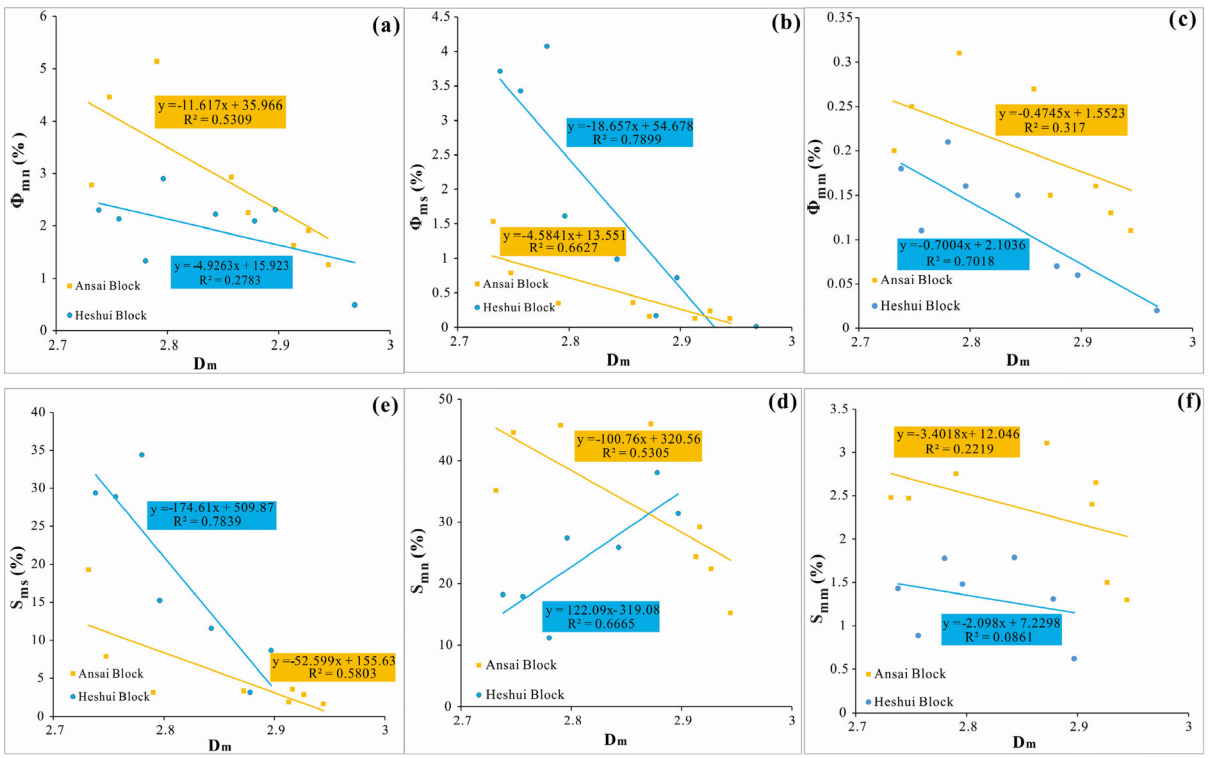

Figure 19. Relationship between fractal dimension D_m and movable fluid distribution parameters. Fractal dimension D_m vs. movable fluid porosity in (**a**) nanoscale pores Φ_{mn}, (**b**) submicron pores Φ_{ms}, (**c**) micron pores Φ_{mm}. Fractal dimension D_m vs. movable fluid saturation in (**d**) nanoscale pores S_{mn}, (**e**) submicron pores S_{ms}, and (**f**) micron pores S_{mm}.

intrusion, scanning electron microscopy, thin section, and X-ray diffraction. The following are the conclusive facts of this research.

1. The Chang 7 sandstone in the study area is a typical tight oil reservoir. The sandstone type in the Heshui Block is mainly feldspar lithic

fragment sandstone, while that in the Ansai Block is primarily lithic fragment feldspar sandstone and feldspar sandstone. The main mineral composition of the Chang 7 sandstone is quartz, feldspar, and clay. The mineral composition in the Heshui Block is different from that of the Ansai Block. In contrast, the sandstone in the Heshui Block has high content of quartz, while that in the Ansai Block has high content of feldspar and clay. Microscopic observation showed five categories of pores: (1) inter-granular dissolution pores; (2) intra-granular dissolution pores; (3) residual inter-granular pores; (4) inter-crystalline pores; and, (5) micro-fractures. Moreover, there were more inter-granular dissolution pores in the Heshui Block than Ansai Block.

2. The PSD, fractal characteristics and movable fluid occurrence in the Heshui Block are different from those in the Ansai Block. The storage space of the Chang 7 sandstone mainly depends on nanoscale pores. There are more nanoscale pores and fewer submicron pores in the Ansai Block than in the Heshui Block. The Chang 7 sandstone is characterized by strong heterogeneity of pore structure. The fractal dimension in the Heshui Block ranges from 2.7318 to 2.9681 (mean 2.8303), and that in the Ansai Block is distributed between 2.7318 and 2.9445 (average 2.8553). Movable fluids are distributed mainly in nanoscale pores, followed by submicron pores. The movable fluid content in the Ansai Block nanoscale pores is higher than in the Heshui Block, while the movable fluid content in submicron pores is lower.
3. Movable fluid distribution is affected by physical properties, mineral composition, pore size and distribution and heterogeneity. The influence of these factors on movable fluid distribution is diverse in different areas. Reservoirs with good physical properties and more submicron pores are often associated with high movable fluid content. High quartz and feldspar content promotes movable fluid occurrence, while clay acts to the contrary. Carbonate is favorable to movable fluid accumulation in the Ansai Block, but not in the Heshui Block. The influence of nanoscale and submicron pores on movable fluid accumulation in the Ansai Block is more significant than in the Heshui Block. The R_{50} can reflect movable fluid distribution better in the Heshui Block than in the Ansai Block. Movable fluid occurrence in nanoscale pores in the Ansai Block is more affected significantly by the heterogeneity than in submicron pores, while it is the opposite in the Heshui Block.

ACKNOWLEDGMENTS

The article's research achievements are funded by the National Natural Science Foundation of China (41872127). We thank the No. 1 and 12 Oil Production Plant, PetroChina Changqing Oilfield Company for providing a database.

REFERENCES

Ajdukiewicz, J. M., & Larese, R. E. (2012). How clay grain coats inhibit quartz cement and preserve porosity in deeply buried sandstones: Observations and experiments. *AAPG Bulletin, 96*, 2091–2119.

Al-Mahrooqi, S. H., Grattoni, C. A., Moss, A. K., & Jing, X. D. (2003). An investigation of the effect of wettability on NMR characteristics of sandstone rock and fluid systems. *Journal of Petroleum Science and Engineering, 39*, 389–398.

Al-Mahrooqi, S. H., Grattoni, C. A., Muggeridge, A. H., Zimmerman, R. W., & Jing, X. D. (2006). Pore-scale modelling of NMR relaxation for the characterization of wettability. *Journal of Petroleum Science and Engineering, 52*, 172–186.

Amadu, M., & Pegg, M. J. (2018). Theoretical and experimental determination of the fractal dimension and pore size distribution index of a porous sample using spontaneous imbibition dynamics theory. *Journal of Petroleum Science and Engineering, 167*, 785–795.

Awan, R. S., Liu, C., Aadil, N., Yasin, Q., Salaam, A., Hussain, A., et al. (2021). Organic geochemical evaluation of Cretaceous Talhar Shale for shale oil and gas potential from Lower Indus Basin, Pakistan. *Journal of Petroleum Science and Engineering, 200*, 108404.

Carr, M. B., Ehrlich, R., Bowers, M. C., & Howard, J. J. (1996). Correlation of porosity types derived from NMR data and thin section image analysis in a carbonate reservoir. *Journal of Petroleum Science and Engineering, 14*, 115–131.

Clarkson, C. R., Freeman, M., He, L., Agamalian, M., Melnichenko, Y. B., Mastalerz, M., et al. (2012a). Characterization of tight gas reservoir pore structure using USANS/SANS and gas adsorption analysis. *Fuel, 95*, 371–385.

Clarkson, C. R., Jensen, J. L., Pedersen, P. K., & Freeman, M. (2012b). Innovative methods for flow-unit and pore-structure analyses in a tight siltstone and shale gas reservoir. *AAPG Bulletin, 96*, 355–374.

Cui, J., Zhu, R., Li, S., Qi, Y., Shi, X., & Mao, Z. (2019a). Development patterns of source rocks in the depression lake basin and its influence on oil accumulation: Case study of the

Chang 7 member of the Triassic Yanchang Formation, Ordos Basin, China. *Journal of Natural Gas Geoscience, 4*, 191–204.
Cui, J., Zhu, R., Luo, Z., & Li, S. (2019b). Sedimentary and geochemical characteristics of the Triassic Chang 7 Member shale in the Southeastern Ordos Basin, Central China. *Petroleum Science, 16*, 285–297.
Dai, C., Cheng, R., Sun, X., Liu, Y., Zhou, H., Wu, Y., et al. (2019). Oil migration in nanometer to micrometer sized pores of tight oil sandstone during dynamic surfactant imbibition with online NMR. *Fuel, 245*, 544–553.
Desbois, G., Urai, J. L., Kukla, P. A., Konstanty, J., & Baerle, C. (2011). High-resolution 3D fabric and porosity model in a tight gas sandstone reservoir: A new approach to investigate microstructures from mm- to nm-scale combining argon beam cross-sectioning and SEM imaging. *Journal of Petroleum Science and Engineering, 78*, 243–257.
Deveugle, P. E. K., Jackson, M. D., Hampson, G. J., Stewart, J., Clough, M. D., Ehighebolo, T., et al. (2014). A comparative study of reservoir modeling techniques and their impact on predicted performance of fluvial-dominated deltaic reservoirs. *AAPG Bulletin, 98*, 729–763.
Dunn, K.-J., Bergman, D. J., & LaTorraca, G. A. (2002). Nuclear magnetic resonance: Petrophysical and logging applications. In K.-J. Dunn, D. J. Bergman, & G. A. LaTorraca (Eds.), *Secondary Nuclear Magnetic Resonance: Petrophysical and Logging Applications.* Elsevier.
Eslami, M., Kadkhodaie-Ilkhchi, A., Sharghi, Y., & Golsanami, N. (2013). Construction of synthetic capillary pressure curves from the joint use of NMR log data and conventional well logs. *Journal of Petroleum Science and Engineering, 111*, 50–58.
Fu, J., Li, S., Xu, L., & Niu, X. (2018). Paleo-sedimentary environmental restoration and its significance of Chang 7 Member of Triassic Yanchang Formation in Ordos Basin, NW China. *Petroleum Exploration and Development, 45*, 988–1008.
Gao, H., & Li, H. (2015). Determination of movable fluid percentage and movable fluid porosity in ultra-low permeability sandstone using nuclear magnetic resonance (NMR) technique. *Journal of Petroleum Science and Engineering, 133*, 258–267.
Hingerl, F. F., Yang, F., Pini, R., Xiao, X., Toney, M. F., Liu, Y., et al. (2016). Characterization of heterogeneity in the Heletz sandstone from core to pore scale and quantification of its impact on multi-phase flow. *International Journal of Greenhouse Gas Control, 48*, 69–83.
Hou, L., Lin, S., & Zhang, L. (2021). New insights from geostatistics on the genetic relationship between shales, mudstones, and sandstones within a parasequence in the lower Chang7 Member of the Upper Triassic Yanchang Formation, Ordos Basin, Northern China. *Journal of Asian Earth Sciences, 213*, 104767.
Huang, H., Li, R., Xiong, F., Hu, H., Sun, W., Jiang, Z., et al. (2020). A method to probe the pore-throat structure of tight reservoirs based on low-field NMR: Insights from a cylindrical pore model. *Marine and Petroleum Geology, 117*, 104344.
Jia, C., Zhang, M., & Zhang, Y. (2012). Unconventional hydrocarbon resources in China and the prospect of exploration and development. *Petroleum Exploration and Development, 39*, 1137–1149.
Katz, A. J., & Thompson, A. H. (1985). Fractal sandstone pores: Implications for conductivity and pore formation. *Physical Review Letters, 54*, 1325–1328.
Kleinberg, R. L. (1996). Utility of NMR T2 distributions, connection with capillary pressure, clay effect, and determination of the surface relaxivity parameter $\rho 2$. *Magnetic Resonance Imaging, 14*, 761–767.
Lai, F., Li, Z., Zhang, W., Dong, H., Kong, F., & Jiang, Z. (2018a). Investigation of pore characteristics and irreducible water saturation of tight reservoir using experimental and theoretical methods. *Energy and Fuels, 32*, 3368–3379.
Lai, J., Wang, G., Ran, Y., Zhou, Z., & Cui, Y. (2016). Impact of diagenesis on the reservoir quality of tight oil sandstones: The case of Upper Triassic Yanchang Formation Chang 7 oil layers in Ordos Basin, China. *Journal of Petroleum Science and Engineering, 145*, 54–65.
Lai, J., Wang, G., Wang, Z., Chen, J., Pang, X., Wang, S., et al. (2018b). A review on pore structure characterization in tight sandstones. *Earth-Science Reviews, 177*, 436–457.
Law, B. E., & Curtis, J. B. (2002). Introduction to unconventional petroleum systems. *The American Association of Petroleum Geologists*.
Li, C., Liu, G., Cao, Z., Yuan, W., Wang, P., & You, Y. (2019a). Analysis of Petrophysical Characteristics and Water Movability of Tight Sandstone Using Low-Field Nuclear Magnetic Resonance. *Natural Resources Research*.
Li, J., Wang, S., Lu, S., Zhang, P., Cai, J., Zhao, J., et al. (2019b). Microdistribution and mobility of water in gas shale: A theoretical and experimental study. *Marine and Petroleum Geology, 102*, 496–507.
Li, P., Sun, W., Wu, B., Gao, Y., & Du, K. (2018a). Occurrence characteristics and influential factors of movable fluids in pores with different structures of Chang 63 reservoir, Huaqing Oilfield, Ordos Basin, China. *Marine and Petroleum Geology, 97*, 480–492.
Li, T., Huang, Z., Feng, Y., Chen, X., Ma, Q., Liu, B., et al. (2020). Reservoir characteristics and evaluation of fluid mobility in organic-rich mixed siliciclastic-carbonate sediments: A case study of the lacustrine Qiketai Formation in Shengbei Sag, Turpan-Hami Basin, Northwest China. *Journal of Petroleum Science and Engineering, 185*, 106667.
Li, Y., Yang, S., Zhao, W., Li, W., & Zhang, J. (2018b). Experimental of hydraulic fracture propagation using fixed-point multistage fracturing in a vertical well in tight sandstone reservoir. *Journal of Petroleum Science and Engineering, 171*, 704–713.
Liu, D., Ren, D., Du, K., Qi, Y., & Ye, F. (2021). Impacts of mineral composition and pore structure on spontaneous imbibition in tight sandstone. *Journal of Petroleum Science and Engineering, 201*, 108397.
Liu, S., & Yang, S. (2000). Upper Triassic – Jurassic sequence stratigraphy and its structural controls in the western Ordos Basin, China. *Basin Research, 12*, 1–18.
Liu, X., Lai, J., Fan, X., Shu, H., Wang, G., Ma, X., et al. (2020a). Insights in the pore structure, fluid mobility and oiliness in oil shales of Paleogene Funing Formation in Subei Basin, China. *Marine and Petroleum Geology, 114*, 104228.
Liu, Y., Yao, Y., Liu, D., Zheng, S., Sun, G., & Chang, Y. (2018). Shale pore size classification: An NMR fluid typing method. *Marine and Petroleum Geology, 96*, 591–601.
Liu, Z., Liu, D., Cai, Y., Yao, Y., Pan, Z., & Zhou, Y. (2020b). Application of nuclear magnetic resonance (NMR) in coalbed methane and shale reservoirs: A review. *International Journal of Coal Geology, 218*, 103261.
Loucks, R. G., & Dutton, S. P. (2019). Insights into deep, onshore Gulf of Mexico Wilcox sandstone pore networks and reservoir quality through the integration of petrographic, porosity and permeability, and mercury injection capillary pressure analyses. *AAPG Bulletin, 103*, 745–765.
Lyu, C., Ning, Z., Wang, Q., & Chen, M. (2018). Application of NMR T2 to pore size distribution and movable fluid distribution in tight sandstones. *Energy and Fuels, 32*, 1395–1405.
Mandelbrot, B. B., Passoja, D. E., & Paullay, D. E. (1984). Fractal character of fracture surfaces in porous media. *Nature, 308*, 721–722.

Mao, G., Lai, F., Li, Z., Wei, H., & Zhou, A. (2020). Characteristics of pore structure of tight gas reservoir and its influence on fluid distribution during fracturing. *Journal of Petroleum Science and Engineering, 193*, 107360.

Mao, Z., He, Y., & Ren, X. (2005). An improved method of using NMR T2 distribution to evaluate pore size distribution. *Chinese Journal of Geophysics, 48*, 412–418.

Mozley, P. S., Heath, J. E., Dewers, T. A., & Bauer, S. J. (2016). Origin and heterogeneity of pore sizes in the Mount Simon Sandstone and Eau Claire Formation: Implications for multiphase fluid flow. *Geosphere, 12*, 1341–1361.

Nie, R.-S., Zhou, J., Chen, Z., Liu, J., & Pan, Y. (2021). Pore structure characterization of tight sandstones via a novel integrated method: A case study of the Sulige gas field, Ordos Basin (Northern China). *Journal of Asian Earth Sciences, 213*, 104739.

Oluwadebi, A. G., Taylor, K. G., & Ma, L. (2019). A case study on 3D characterisation of pore structure in a tight sandstone gas reservoir: The Collyhurst Sandstone, East Irish Sea Basin, northern England. *Journal of Natural Gas Science and Engineering, 68*, 102917.

Qiao, J., Zeng, J., Jiang, S., Ma, Y., Feng, S., Xie, H., et al. (2020a). Role of pore structure in the percolation and storage capacities of deeply buried sandstone reservoirs: A case study of the Junggar Basin, China. *Marine and Petroleum Geology, 113*, 104129.

Qiao, J., Zeng, J., Jiang, S., & Wang, Y. (2020b). Impacts of sedimentology and diagenesis on pore structure and reservoir quality in tight oil sandstone reservoirs: Implications for macroscopic and microscopic heterogeneities. *Marine and Petroleum Geology, 111*, 279–300.

Qiao, J., Zeng, J., Ma, Y., Jiang, S., Feng, S., & Hu, H. (2020c). Effects of mineralogy on pore structure and fluid flow capacity of deeply buried sandstone reservoirs with a case study in the Junggar Basin. *Journal of Petroleum Science and Engineering, 189*, 106986.

Rezaee, R., Saeedi, A., & Clennell, B. (2012). Tight gas sands permeability estimation from mercury injection capillary pressure and nuclear magnetic resonance data. *Journal of Petroleum Science and Engineering, 88–89*, 92–99.

Rosenbrand, E., Fabricius, I. L., Fisher, Q., & Grattoni, C. (2015). Permeability in Rotliegend gas sandstones to gas and brine as predicted from NMR, mercury injection and image analysis. *Marine and Petroleum Geology, 64*, 189–202.

Schmitt, M., Halisch, M., Müller, C., & Fernandes, C. P. (2016). Classification and quantification of pore shapes in sandstone reservoir rocks with 3-D X-ray micro-computed tomography. *Solid Earth, 7*, 285–300.

Schmitt Rahner, M., Halisch, M., Peres Fernandes, C., Weller, A., Santiago, S., & dos Santos, V. (2018). Fractal dimensions of pore spaces in unconventional reservoir rocks using X-ray nano- and micro-computed tomography. *Journal of Natural Gas Science and Engineering, 55*, 298–311.

Shabaninejad, M., Middlelton, J., & Fogden, A. (2018). Systematic pore-scale study of low salinity recovery from Berea sandstone analyzed by micro-CT. *Journal of Petroleum Science and Engineering, 163*, 283–294.

Shanley, K. W., Cluff, R. M., & Robinson, J. W. (2004). Factors controlling prolific gas production from low-permeability sandstone reservoirs: Implications for resource assessment, prospect development, and risk analysis. *AAPG Bulletin, 88*, 1083–1121.

Shao, X., Pang, X., Li, H., & Zhang, X. (2017). Fractal analysis of pore network in tight gas sandstones using NMR method: A case study from the Ordos Basin, China. *Energy and Fuels, 31*, 10358–10368.

Sun, W., Zuo, Y., Wu, Z., Liu, H., Xi, S., Shui, Y., et al. (2019). Fractal analysis of pores and the pore structure of the Lower Cambrian Niutitang shale in northern Guizhou province: Investigations using NMR, SEM and image analyses. *Marine and Petroleum Geology, 99*, 416–428.

Tahir, M., Awan, R., Muzaffar, W., & Iltaf, K. (2020). Organic geochemical evaluation of the Lower Cretaceous Sembar Formation to identify shale-gas potential from the southern Indus Basin Pakistan. *N Am Acad Res, 3*, 54–78.

Taylor, T. R., Giles, M. R., Hathon, L. A., Diggs, T. N., Braunsdorf, N. R., Birbiglia, G. V., et al. (2010). Sandstone diagenesis and reservoir quality prediction: Models, myths, and reality. *AAPG Bulletin, 94*, 1093–1132.

Testamanti, M. N., & Rezaee, R. (2017). Determination of NMR T2 cut-off for clay bound water in shales: A case study of Carynginia Formation, Perth Basin, Western Australia. *Journal of Petroleum Science and Engineering, 149*, 497–503.

Thomson, P.-R., Jefferd, M., Clark, B. L., Chiarella, D., Mitchell, T. M., & Hier-Majumder, S. (2020). Pore network analysis of Brae Formation sandstone, North Sea. *Marine and Petroleum Geology, 122*, 104614.

Tian, L., Yang, D., Zheng, S., & Feng, B. (2018). Parametric optimization of vector well patterns for hydraulically fractured horizontal wells in tight sandstone reservoirs. *Journal of Petroleum Science and Engineering, 162*, 469–479.

Tian, W., Lu, S., Huang, W., Wang, S., Gao, Y., Wang, W., et al. (2019). Study on the full-range pore size distribution and the movable oil distribution in glutenite. *Energy and Fuels, 33*, 7028–7042.

Timur, A. (1969). Pulsed nuclear magnetic resonance studies of porosity, movable fluid, and permeability of sandstones. *Journal of Petroleum Technology, 6*, 775–786.

Wang, F., & Zeng, F. (2020). Novel insights into the movable fluid distribution in tight sandstones using nuclear magnetic resonance and rate-controlled porosimetry. *Natural Resources Research, 29*, 3351–3361.

Wang, F., Zeng, F., Wang, L., Hou, X., Cheng, H., & Gao, J. (2021). Fractal analysis of tight sandstone petrophysical properties in unconventional oil reservoirs with nmr and rate-controlled porosimetry. *Energy and Fuels, 35*, 3753–3765.

Worden, R. H., Bukar, M., & Shell, P. (2018). The effect of oil emplacement on quartz cementation in a deeply buried sandstone reservoir. *AAPG Bulletin, 102*, 49–75.

Wu, J., Fan, T., Gomez-Rivas, E., Travé, A., Gao, Z., Wang, S., et al. (2021). Fractal characteristics of pore networks and sealing capacity of Ordovician carbonate cap rocks: A case study based on outcrop analogues from the Tarim Basin, China. *AAPG Bulletin, 105*, 437–479.

Wu, Y., Tahmasebi, P., Lin, C., Zahid, M. A., Dong, C., Golab, A. N., et al. (2019). A comprehensive study on geometric, topological and fractal characterizations of pore systems in low-permeability reservoirs based on SEM, MICP, NMR, and X-ray CT experiments. *Marine and Petroleum Geology, 103*, 12–28.

Yan, J., He, X., Zhang, S., Feng, C., Wang, J., Hu, Q., et al. (2020). Sensitive parameters of NMR T2 spectrum and their application to pore structure characterization and evaluation in logging profile: A case study from Chang 7 in the Yanchang Formation, Heshui area, Ordos Basin, NW China. *Marine and Petroleum Geology, 111*, 230–239.

Yang, L., Wang, S., Jiang, Q., You, Y., & Gao, J. (2020). Effects of microstructure and rock mineralogy on movable fluid saturation in tight reservoirs. *Energy and Fuels, 34*, 14515–14526.

Yang, Y., Li, W., & Ma, L. (2005). Tectonic and stratigraphic controls of hydrocarbon systems in the Ordos basin: A multicycle cratonic basin in central China. *AAPG Bulletin, 89*, 255–269.

Yao, Y., & Liu, D. (2012). Comparison of low-field NMR and mercury intrusion porosimetry in characterizing pore size distributions of coals. *Fuel, 95*, 152–158.

Yao, Y., Liu, D., Che, Y., Tang, D., Tang, S., & Huang, W. (2010). Petrophysical characterization of coals by low-field nuclear magnetic resonance (NMR). *Fuel, 89*, 1371–1380.

Yin, S., Dong, L., Yang, X., & Wang, R. (2020). Experimental investigation of the petrophysical properties, minerals, elements and pore structures in tight sandstones. *Journal of Natural Gas Science and Engineering, 76*, 103189.

Yuan, X., Lin, S., Liu, Q., Yao, J., Wang, L., Guo, H., et al. (2015). Lacustrine fine-grained sedimentary features and organicrich shale distribution pattern: A case study of Chang 7 Member of Triassic Yanchang Formation in Ordos Basin, NW China. *Petroleum Exploration and Development, 42*, 37–47.

Zha, M., Wang, S., Ding, X., Feng, Q., Xue, H., & Su, Y. (2019). Tight oil accumulation mechanisms of the Lucaogou Formation in the Jimsar Sag, NW China: Insights from pore network modeling and physical experiments. *Journal of Asian Earth Sciences, 178*, 204–215.

Zhang, F., Jiang, Z., Sun, W., Li, Y., Zhang, X., Zhu, L., et al. (2019a). A multiscale comprehensive study on pore structure of tight sandstone reservoir realized by nuclear magnetic resonance, high pressure mercury injection and constant-rate mercury injection penetration test. *Marine and Petroleum Geology, 109*, 208–222.

Zhang, J., Wei, C., Ju, W., Qin, Z., Ji, Y., Quan, F., et al. (2020a). Microscopic distribution and dynamic variation of water under stress in middle and high rank coal samples. *Journal of Natural Gas Science and Engineering, 79*, 103369.

Zhang, J., Wei, C., Ju, W., Yan, G., Lu, G., Hou, X., et al. (2019b). Stress sensitivity characterization and heterogeneous variation of the pore-fracture system in middle-high rank coals reservoir based on NMR experiments. *Fuel, 238*, 331–344.

Zhang, K., Liu, R., Liu, Z., Li, B., Han, J., & Zhao, K. (2020b). Influence of volcanic and hydrothermal activity on organic matter enrichment in the Upper Triassic Yanchang Formation, southern Ordos Basin, Central China. *Marine and Petroleum Geology, 112*, 104059.

Zhang, Z., & Andreas, W. (2014). Fractal dimension of pore-space geometry of an Eocene sandstone formation. *Geophysics, 79*, D377–D387.

Zhao, Y., Lin, B., Liu, T., Zheng, Y., Sun, Y., Zhang, G., et al. (2021). Multifractal analysis of coal pore structure based on NMR experiment: A new method for predicting T2 cutoff value. *Fuel, 283*, 119338.

Zhou, S., Liu, D., Cai, Y., & Yao, Y. (2016a). Fractal characterization of pore–fracture in low-rank coals using a low-field NMR relaxation method. *Fuel, 181*, 218–226.

Zhou, Y., Ji, Y., Xu, L., Che, S., Niu, X., Wan, L., et al. (2016b). Controls on reservoir heterogeneity of tight sand oil reservoirs in Upper Triassic Yanchang Formation in Longdong Area, southwest Ordos Basin, China: Implications for reservoir quality prediction and oil accumulation. *Marine and Petroleum Geology, 78*, 110–135.

Zou, C., Zhu, R., Liu, K., Su, L., Bai, B., Zhang, X., et al. (2012). Tight gas sandstone reservoirs in China: Characteristics and recognition criteria. *Journal of Petroleum Science and Engineering, 88–89*, 82–91.

Zou, M., Liu, Y., Huang, Z., Zhang, M., & Zhang, P. (2020). Geological control of irreducible water within the coal matrix and its quantified evaluation model. *ACS Omega, 5*, 9540–9549.